UNIVERSITY OF CALIFORNIA
RIVERSIDE

Extended Hubbard Model: Studies on Quantum Information and Disorder

A Dissertation submitted in partial satisfaction
of the requirements for the degree of

Doctor of Philosophy

in

Physics

by

Jon David Spalding

September 2020

Dissertation Committee:

Dr. Shan-Wen Tsai, Chairperson
Dr. Michael Mulligan
Dr. Leonid Pryadko

The Dissertation of Jon David Spalding is approved:

Committee Chairperson

University of California, Riverside

Acknowledgments

This thesis includes contents previously published by the author, in the paper [1],

J. Spalding, S.-W. Tsai, and D. K. Campbell, "Critical entanglement for the half-filledextended hubbard model", Phys. Rev. B99, 195445 (2019

UCSD's COMET cluster

UCR's HPCC

Ka-Ming Tam and his unfinished works and willingness to let me finish them

David Campbell's excitement for EHM and Solitons

GRMP fellowship in 2016

Steve White's DMRG class 2016.

Miles Stoudenmire for setting up ITensor and answering questions

Dr. Michael Philipps for providing this LaTex thesis template

John Cardy for answering my email and making BKT transitions exciting for me

Dr. Michael Maroun and Professor Lapidus for encouraging my mathematical wanderlust and letting me come to his birthday party in San Luis Obispo

Box Springs Mountain, where I was living in a cave for the duration of my PhD near the Two Trees springs. I've buried a time capsule in one of the caves, think you can find it?

Dedication:

To the adventure of Physics, and to all the explorers present and past whose achievements inspire me to do stupid and exciting things.

Abstract of the Dissertation

Extended Hubbard Model: Studies on Quantum Information and Disorder

by

Jon David Spalding

Doctor of Philosophy, Graduate Program in Physics
University of California, Riverside, September 2020
Dr. Shan-Wen Tsai, Chairperson

The simplest way to add interactions to a single-band model of spinful electrons hopping on a crystal lattice is the Hubbard model, and the next simplest model is the extended Hubbard model (EHM). The EHM is useful for modeling superconductive electron pairing and emergent insulating phases including a dimerized phase called the "Bond Order Wave". In this thesis, I present two projects. In the first, I applied the numerical method of Density Matrix Renormalization Group to study the entanglement entropy at critical points of the clean EHM in one dimension near the BOW phase. In the second project, I applied analytical renormalization group approaches to study the phase diagram of the one dimensional model with weak disorder at weak coupling.

Contents

List of Figures

List of Tables

Part I

A Numerical Study of the Extended Hubbard Model

Chapter 1

Introduction

The one-dimensional Hubbard model is the minimal model for the study of interacting fermions with spin [2] and has applications in a number of effectively one-dimensional materials including organic conductors, conjugated polymers, and carbon nanotubes [3–6] as well as quantum simulators including fermionic cold-atoms [7–10] and now quantum dot arrays [11]. At least in the cold-atom experiments, methods have been demonstrated for measuring the 2^{nd} Renyi entropy [12].

In addition to the 2^{nd} Renyi entropy, many other measures of entanglement have been conceived as means of characterizing the quantum-mechanical properties of interacting many-body systems. The most well-established, the von-Neumann entanglement entropy, is the focus of this paper, but our analysis extends to the higher Renyi entropies. The von-Neumann entanglement entropy is defined as

$$S_{vN}(x) = \mathrm{Tr}_A \left(\rho_B \log(\rho_B)\right) \tag{1.1}$$

where $x \in (0, L)$ defines a spatial bipartition of the wavefuction into subsystem A and subsystem B, and $\rho_{A(B)}$ represents the density matrix for subsystem A(B). $S_{vN}(x)$ quantifies the inability to write the wavefunction as a simple product over single-particle states in the spatial basis. At quantum criticality, the focus of this paper, $S_{vN}(x)$ grows logarithmically for ground state many-body wavefunctions. The importance of quantum-information to many-body physics is most apparent in the modern Matrix Product State formulation of the Density Matrix Renormalization Group (DMRG) method [13, 14]. As a variational method, DMRG includes a tensor network bond dimension (referred to here as M) that sets the amount of quantum information to keep during the ground state optimization [15].

By adding to the Hubbard model a term for interactions between electrons on neighboring sites, the Hubbard model becomes the Extended Hubbard Model (EHM), which has been simulated using gated quantum dot arrays [11]. The nearest-neighbor interaction may also be simulated using cold dipolar atoms [16–21] and polar molecules [22–28] in one-dimensional optical lattices. The EHM is described by the Hamiltonian

$$\begin{aligned} H_{EHM} = & -t \sum_{i,s} (c^\dagger_{i,s} c_{i+1,s} + c^\dagger_{i+1,s} c_{i,s}) \\ & + U \sum_i n_{i,\uparrow} n_{i,\downarrow} + V \sum_i n_i n_{i+1} \end{aligned} \tag{1.2}$$

where in second-quantized notation, $n_i = n_{i,\uparrow} + n_{i,\downarrow}$ represents the site occupancy, $c^\dagger_{i,s}$ ($c_{i,s}$) represents a creation (annihilation) operator with spin s, and we set $t = 1$ throughout this

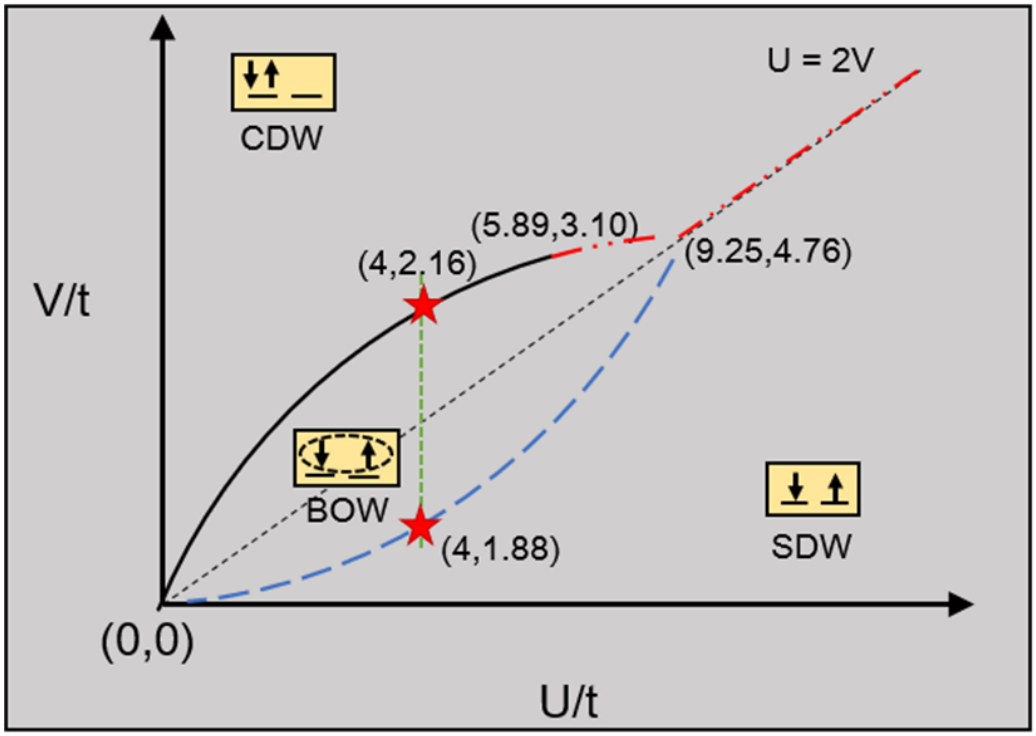

Figure 1.1: A schematic of the known phase diagram in the repulsive region of the 1D extended Hubbard model at half filling. We focus on the two starred critical points: a BKT point at (4,1.88) and a Gaussian transition at (4,2.16). The blue, single dash represents BKT transitions that span from the origin to the multicritical point (9.25,4.76). The red dash-dot-dot lines represent 1^{st}-order transitions, and the black solid curve is a set of second-order transitions. The black solid and red dash-dot-dot curves meet at (5.89, 3.10). Values are from reference [3].

paper. This model hosts highly nontrivial many-body physics, even in one dimension, and cannot be studied using analytical means at intermediate coupling.

The phase diagram for the half-filled, repulsive case shown in figure 1.1 has been studied and repeatedly updated over four-decades of investigations and became hotly debated once compelling evidence for a thin Bond Order Wave (BOW) region was demonstrated with exact diagonalization and later renormalization group arguments [29–31] (for clarity the region is magnified here in figure 1.1). The BOW phase is characterized by a ground state with gapped excitations and alternating bonds between neighboring sites; it is separated from a Spin Density Wave (SDW) region by a Berezinskii-Kosterlitz-Thouless (BKT) transition and from a Charge Density Wave (CDW) region by a second-order transition curve that changes at a tricritical point into a 1^{st}-order transition before terminating at a multicritical point [3, 29, 32–38]. In this study, we restrict ourselves to U = 4 in an effort to identify the second-order critical point, herein referred to as V_{Gauss}, and the BKT-critical point, V_{BKT} (denoted by star symbols in figure 1.1).

The phase diagram has been studied with a wide range of methods and has motivated innovations such as parallel tempering for Quantum Monte Carlo (QMC) [33]. The studies based on DMRG have gradually improved independently of the developments in QMC. Starting in 2002, an early study concluded that the BOW phase appears infinitesimally close to the line U = 2V. This work used the relatively high bond dimension (M) of 1200 and system sizes up to L = 1024 sites [39]. In another DMRG study in 2004, the BKT transition was predicted [34] to be at V = 2.01 as extrapolated from moderate (96 to 256) system sizes using peaks in the BOW structure factor, but with the relatively low M

of only 500. In 2007, large L up to 1000 and large M up to 3000 were used to locate this transition at $V_{BKT} \approx 1.877$ using standard order-parameter approaches scaled in L [3] which agreed closely with the high-accuracy QMC result of $V_{BKT} = 1.89(1)$ [33]. More recently in 2015, with M $\leq$ 1024 and L $\leq$ 180 with open boundaries, a careful study used a finite-size corrected spin-gap at U = 4 to get $V_{BKT} = 2.08$ [40] which adds controversy to this difficult-to-locate BKT critical point. Note that in general, scaling DMRG measurements in L or M can each fail outside of critical regions of (L,M)-space [41] which likely accounts for the inconsistencies of prior works. We avoided these issues through very conservative DMRG convergence as well as checking the consistency of results with different M for fixed L.

A recent study [42] using a continuous unitary transformation (CUT) approach [43] agrees with the numerical values for the CDW/BOW transition and interprets that transition as the condensation of singlet excitons [42].

The phase transitions shown in figure 1.1 have previously been studied using transition measures based on quantum mechanical many-body properties. Energy-level-crossing methods such as "fidelity susceptibility" and "excited state fidelity" can accurately identify phase transitions [44], and entanglement has been demonstrated as a central tool in the study of quantum phase transitions [45]. Peaks and discontinuities in various entanglement entropies are useful for models with no *a-priori* order parameter. The half-chain von-Neumann entanglement entropy (from now on, we refer to the von-Neumann entanglement entropy as simply the "entropy"), 2-site entropy, and 1-site entropy were previously computed using DMRG to produce an Extended Hubbard model ground state phase dia-

gram [46]. The different methods agreed with Refs. [3, 33] with some small discrepancies. These discrepancies can, we conclude, be overcome in the EHM using universal results from conformal field theory, previously applied to identification of BKT transitions in the J_1-J_2 model from the ground state entanglement with periodic boundary conditions (PBC) [47]. In this paper we extend the method demonstrated in Ref. [47] to open boundary conditions (OBC) for the EHM by taking a logarithmic derivative of the entropy for even and odd sites seperately before averaging them to overcome the bond-alternation effects. Using the peak in the central charge, we feel we have successfully identified the BKT transition.

Recently, a direct curve fit of the CFT predictions was used to study small lattices, to demonstrate the feasibility of detecting the central charge and the Luttinger exponent directly from the 2^{nd} Renyi entropy in cold-atom experiments [48]. In Refs. [49, 50], CFT predictions were verified for a one-dimensional bosonic Hamiltonian that acts as a quantum simulator for the O(2) model in 1+1 dimensions, using the midpoint of the chain as the optimal location to sample the open-boundary DMRG ground state because there the finite-size effects as well as boundary effects are minimized, a feature previously exploited in Ref. [51]. However, extracting useful information at the chain midpoint requires a large number of system sizes.

Likewise, it may be prohibitive to repeat an experiment with multiple system sizes, and one-dimensional lattice experiments will usually have a symmetric but inhomogeneous confining potential. Hence for any numerical or experimental 1D critical models with open boundaries, especially with symmetric but non-uniform potentials, the methods we develop below, which we call "scaling to the middle," should be of value for extracting the most

accurate measurements at the midpoint. In short, we re-fit the universal CFT formula for entropy at a 1D quantum critical point to open boundary entropy data for every possible domain centered on the chain midpoint, before extrapolating the curve fit parameters to a domain of 0. This is effectively scaling the curve fitted values in the size of the system block. For the EHM, we combine this curve-fitting algorithm with a simple variance minimum for the CFT curve fit to identify a Gaussian critical point (V_{Gauss}) with high accuracy for small system sizes. Compare our value of $V_{Gauss} = 2.158$ (2.160) from a 64 (128)-site lattice OBC calculation to the best published values of 2.160 from 1000-site QMC [33] and 2.164 from 1000-site DMRG [52]. We postpone further application and validation of the method, including inhomogeneous potentials, to a future work focused on a simpler model. At the BKT point, our best result is based on curve fitting to extract the central charge maximum before scaling in 1/L for the largest systems (128 and 256) to yield $V_{BKT} = 1.91(3)$. This compares well to our favorite published values of 1.877 and 1.89(1) [3] [33] especially considering that our methods have never been attempted in this setting before and that our system sizes are limited.

In this study, we demonstrate our approaches to finding critical points with OBC ground states and apply them to the EHM at half-filling with a cut along the phase diagram at U = 4. Along the way, we expand upon the method developed in Ref. [47] for identifying BKT critical points, but for open-boundary wavefunctions, demonstrated by identifying V_{BKT} for our model. We characterize the nature of finite-size and boundary effects that occur for this model at V_{Gauss} and in the CDW phase. This includes observations of a degeneracy-induced charge soliton that increases the CFT central charge from 1 to 2 at

V_{Gauss}, and simple on-site U pinning to eliminate it for both OBC and PBC. We also observe a growth of entropy oscillations away from open boundaries at V_{Gauss}, contradicting the usual decay of oscillations as observed for Luttinger Liquids, due to the same CDW soliton that increases c from 1 to 2.

Chapter 2

Methods

The existence of a mapping between classical critical points in two dimensions and quantum critical points in one dimension implies that the results of conformal field theory also apply for one-dimensional quantum critical points [53–55].

Using this mapping and field theory techniques, it was shown that the entanglement entropy of quantum critical points takes a logarithmic form [56–58], and for open boundaries, the ground state entanglement entropy was derived using CFT as [59]

$$S_{vN} = S_0 + \frac{c}{6} \log \left(\frac{2L}{\pi} \sin \frac{\pi x}{L}\right) \tag{2.1}$$

For periodic boundaries, the factor of 1/6 is replaced with a factor of 1/3 and the 2L changes to L. It was later shown numerically that the entropy takes the form [60]

$$S_{vN} = S_0 + \frac{c}{6} \log \left(\frac{2L}{\pi} \sin \frac{\pi x}{L}\right) + \frac{\alpha(-1)^x}{\left(\frac{2L}{\pi} \sin \frac{\pi x}{L}\right)^K} \tag{2.2}$$

for systems with open boundaries [61]. Although the oscillatory term doesn't appear in the Von-Neumann entropy with PBC, it does appear for Renyi entropies, and this can add a

coefficient to K [49]. The coefficient α is non-universal, and in subsequent tables 3.1 and 3.2 we replace the overall coefficient on the oscillatory term with $A \equiv \frac{\alpha}{(2L/\pi)^K}$.

These details are important for interpreting numerical results. Note that the third term predicts a decay of oscillations away from the boundary, with a universal exponent K called the Luttinger exponent. The Luttinger exponent appears analytically in the weak-coupling bosonization treatment of equation (1.2) [31]. Even though the analytical bosonization treatment fails at intermediate couplings, the Luttinger Liquid picture is expected to hold in all the critical phases we studied.

2.1 *Scaling to the middle* for improved measurements

Since the DMRG is best with open boundaries, but open boundaries induce various edge effects, it is desirable to take measurements at or near the midpoint of a lattice [49–51]. Many open-boundary effects may be improved by performing measurements at the midpoint for many L and then scaling in L [60].

Here we test a complementary approach that improves the accuracy for any single-system-size curve fit measurement performed on open boundary condition data [60, 62, 63] and explain it through an example.

We illustrate the method by computing central charge for a 64-site lattice in the critical SDW phase, at U = 4 and V = 1, which is expected to have similar entropy to the critical antiferromagnetic XXZ model with open boundaries. We remind the reader that the entire SDW phase is characterized by the strong-U Hubbard model, which in the infinite-U

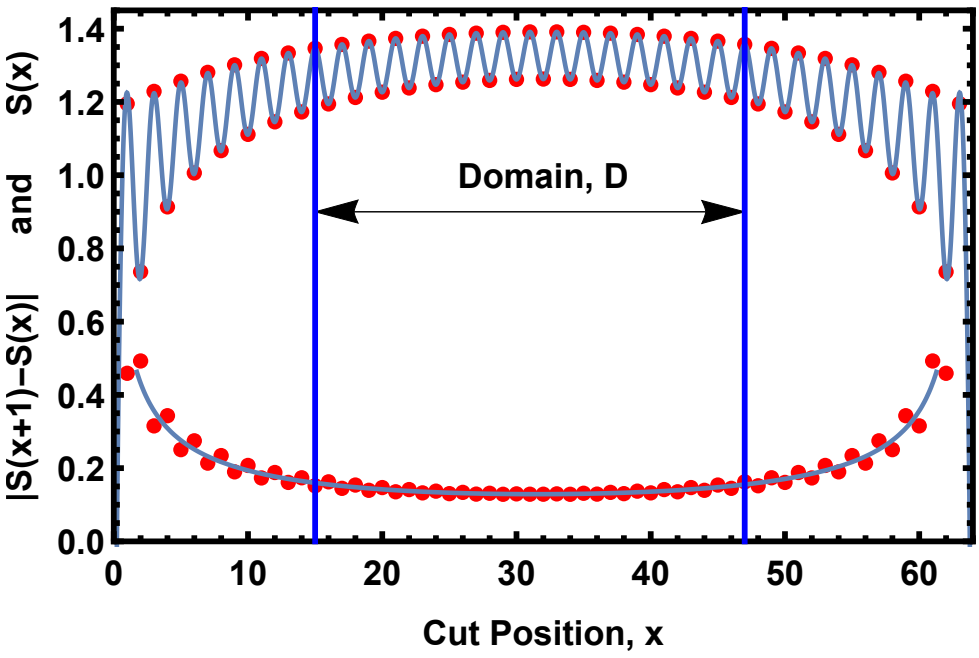

Figure 2.1: "Domain, D" defined for curve fitting the entropy. Here U = 4 and V = 1 in the SDW phase and compares well to a critical antiferromagnetic XXZ spin chain [60]. For comparison to figure 3.1, the curve fit for D = 32 is plotted in blue. Below that, we show the absolute value of the oscillations along with the oscillatory part of the curve fit.

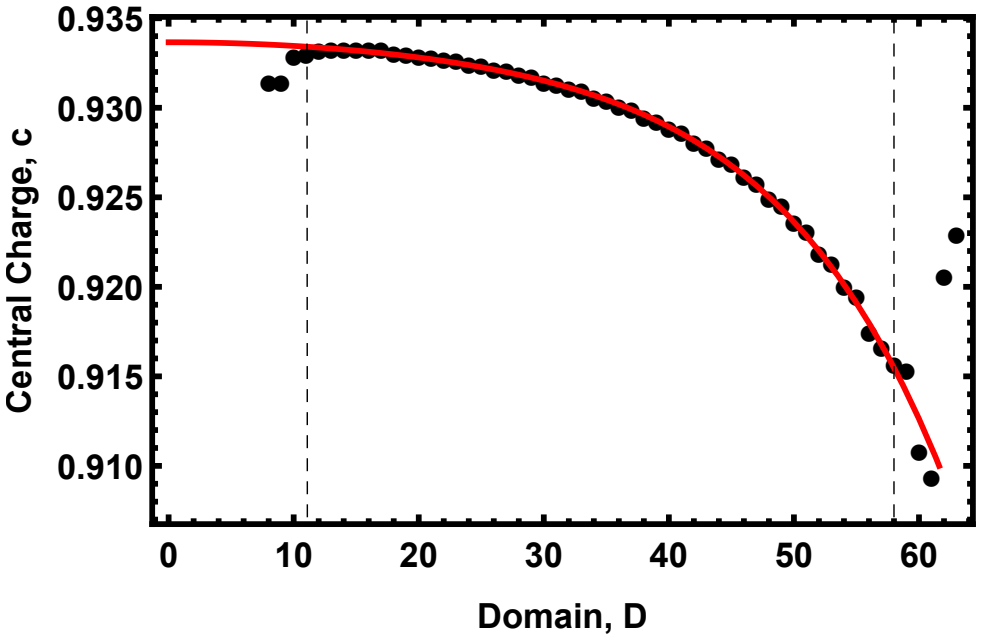

Figure 2.2: "Scaling to the Middle" applied to measuring c when U = 4 and V = 1 for L = 64. A curve fit is performed for each domain, D as in figure 2.1, resulting in a value of central charge, $c(D)$. The values are extrapolated to domain 0 to produce a best estimate value.

limit becomes the Heisenberg model. The critical entanglement entropy of the antiferromagnetic XXZ model with OBC was studied for the first time in reference [60], which is the source for equation 2.2. Indeed, S(x) for the SDW in figure 2.1 exhibits an algebraic decay of entropy oscillations away from the boundaries superimposed on logarithmic growth of entropy away from the boundary, in full agreement with equation 2.2 [1].

Figure 2.1 shows the centered domain D, which is curve fitted by equation 2.2 to extract a value of c(D). This is repeated for all D before fitting the values of c vs D using an even function. By evaluating this c(D) curve fit at D = 0, we can extract a "best value" for this lattice size as illustrated in figure 2.2. This method of measuring c removes the ambiguity over which is the best domain for curve fitting equation 2.2 with open boundaries. Note that overfitting and strong edge effects are clearly visible in the plot of c(D), and allow one to quickly select which values of D are used in the curve fit.

Lastly, we comment that figure 2.3 demonstrates the utility of "scaling to the middle" in checking finite-size and curve-fit domain effects. It shows the unsuccessful results of locating V_{BKT} using the variance minimum and scaling to the middle for entropy fit 2.2. This equation is lacking in higher order corrections that are needed at V_{BKT}. We discuss this failure further in the next section.

2.2 *Variance minimum* for finding critical points

The conformal entropy formula 2.2 only fits at critical points. Therefore, a plot of any measure of the quality of the curve fit, as a function of coupling constants along a

[1] The Variance is low for the entire SDW phase; see figure 2.4

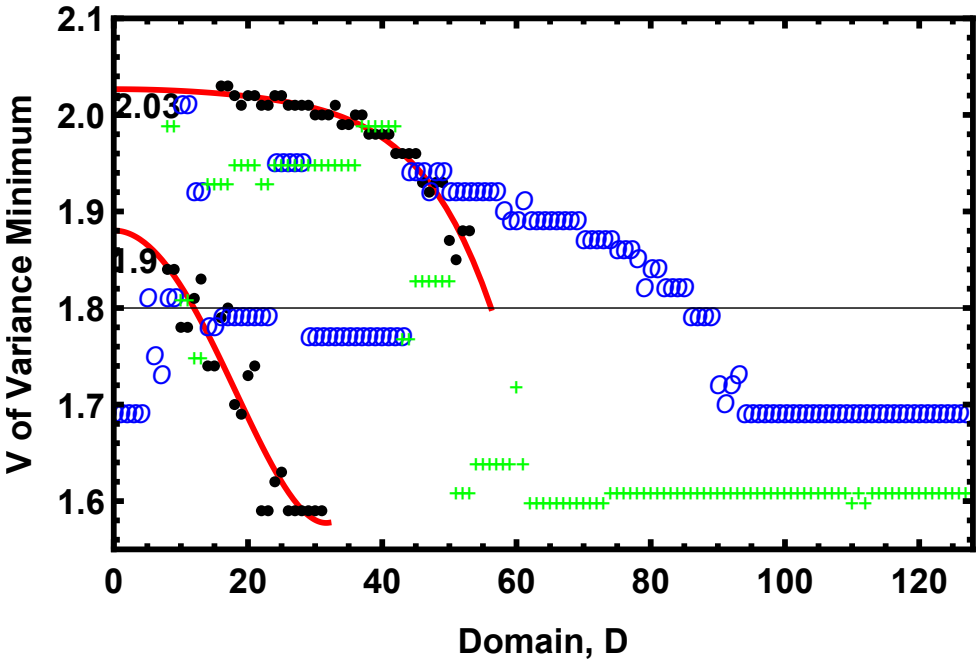

Figure 2.3: Variance minimum vs domain for L = 32 (lower red curve and black dots), 64 (upper red curve and black dots), 128 (blue "O"), and 256 sites (green "+"). Shows that the variance minimum does not work for equation 2.2 when applied at the BKT point, as expected due to marginal corrections.

cut in the phase diagram, will exhibit a clear minimum when such a critical point separates two gapped phases (for instance, along U = 4 from BOW to CDW). Here we used the "Estimated Variance", or just "Variance", defined as

$$variance \equiv \sum_{i=1}^{D} \frac{(y_i - \hat{y}_i)^2}{D - p} \tag{2.3}$$

where D is the number of data points included in the curve fit (also the domain) and p is the number of curve fit parameters; y_i is a data point and $\hat{y}_i$ is the corresponding value predicted with the curve fit, and y_i - $\hat{y}_i$ is a residual [2]. From now on we refer to this as the variance of the curve fit.

This works very well for all of the system sizes we studied and provides an extremely sharp, reliable transition indicator, with very low error even for small system sizes, as illustrated for 16 sites in figure 2.4. This plot was generated by fixing D to the middle half of the data. Figure 2.5 which shows the entropy at the 5 regions of interest in figure 2.4, that is, the SDW phase, the BOW phase, the CDW phase twice (V $\approx$ 2.5 and 3), and the two critical points including the apparent BKT point. All of the features in figure 2.5 are studied in greater detail later on.

We can combine the "Scaling to the middle" technique with the "Variance Minimum" method, as shown in figure 2.6. Each of the data points in that figure is the V_{Gauss} corresponding to the variance minimum for a particular D (example variance in the inset). This collection of critical points is then curve fitted and extrapolated to an effective D of 0. This final step requires care, since if D is too small, overfitting disrupts the curve fit,

[2]The "Estimated Variance" is implemented in Mathematica's NonlinearModelFit function, and is generated automatically.

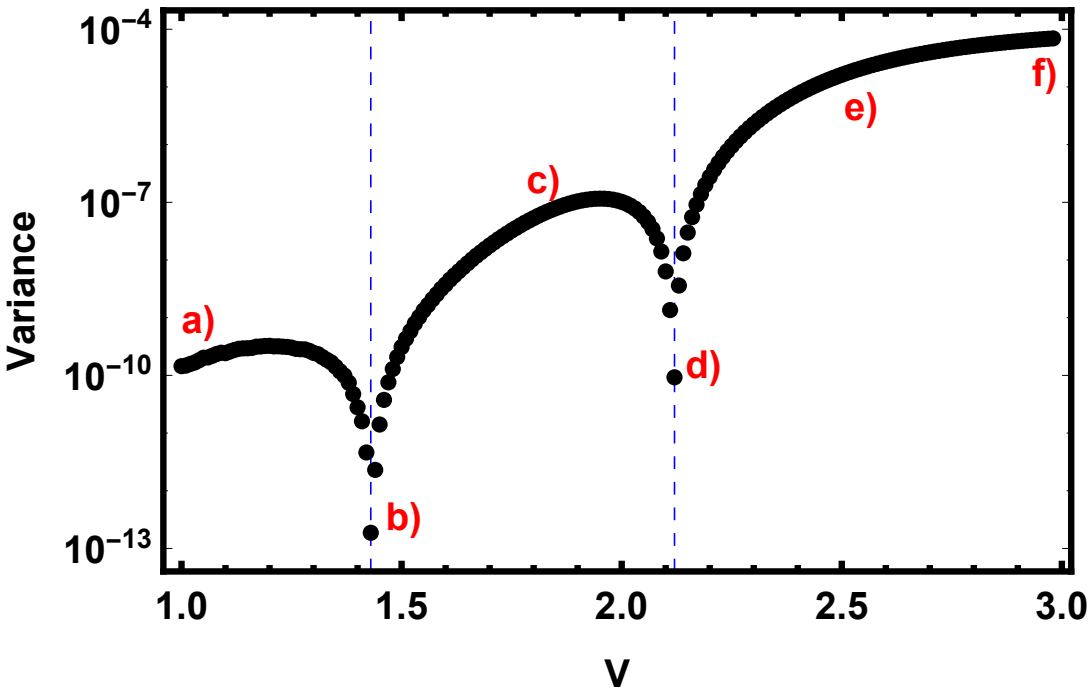

Figure 2.4: Variance vs V for 16 sites, with local minima at 1.43 and 2.12 using a domain of 8 sites. 2.12 is 0.04 above the result published in Ref. [34] which were generated using much larger system sizes. The lettered points in this figure correspond to the labels in figure 2.5.

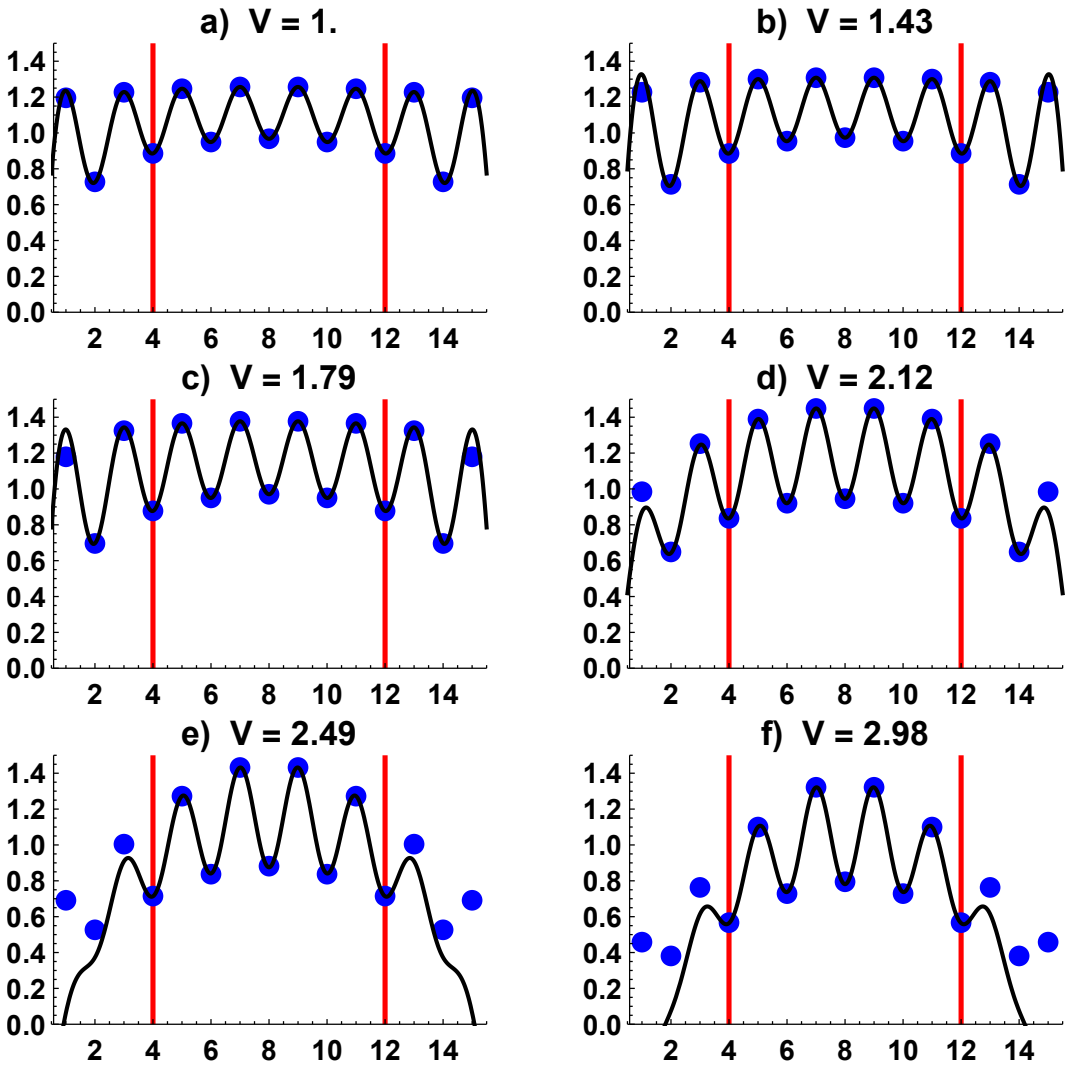

Figure 2.5: Entropy for L = 16 with a CFT curve fit (black curves) for representative values of V from figure 2.4, including the two local minima. Red bars indicate the domain of the curve fit.

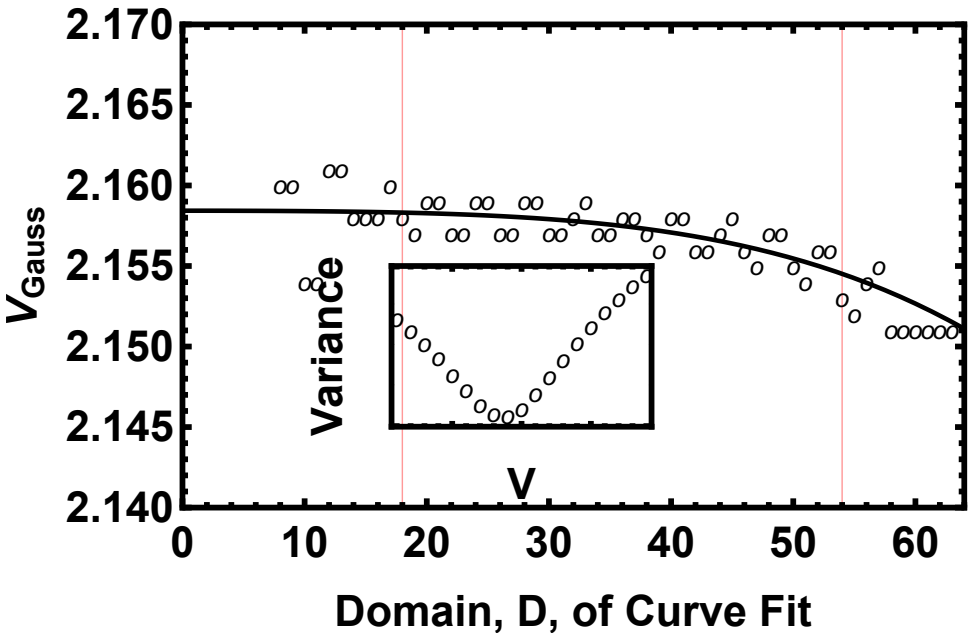

Figure 2.6: Illustration of the combined "scaling to the middle" and "variance minimum" procedure applied to identifying a critical point for 64-site data. The constant term in the polynomial fit is the value of interest; in this case it is the critical point, V_{Gauss}. First, for each domain D, the minimum variance is used to identify the critical point (shown in subplot) and these critical points are then fitted as a function of D with an even polynomial. The constant in the curve fit, here 2.158, is the best estimate for the critical point. A conservative error estimate is ± 0.001.

and when D is too large, edge effects disrupt the curve fit, so the curve fit is restricted to the smooth part of the data. This step requires visual inspection of the data. Contrast figure 2.6, demonstrating the successful extrapolation of V_{Gauss} using scaling to the middle, with figure 2.3; in the former, a clear convergence in D is visible, and this convergence is consistent for all system sizes (see table 3.1); in the latter, there is no convergence in D for larger systems, and the different sizes disagree with each other.

The method worked well when there is a transition from gapped to gapped phases separated by a gapless transition point. Yet the BKT phase transition point divides a

gapless *region* from a gapped region, so that the variance is not expected to produce a clear minimum. Rather, we hoped for some kind of a step feature. Unexpectedly, we still found a minimum in our data (figure 2.4) that we pursued to its dead end.

The evidence that the combined Variance Minimum and Scaling to the Middle method is failing in this case comes in two forms: first, the value of interest changes drastically or is wildly inconsistent for different domains. In figure 2.3, V_{BKT} shifts from 1.6 to 1.9 for 32 sites and 1.8 to 2.03 for 64 sites, and then appears to oscillate as a function of D for the other two data sets. These wild oscillations don't appear, for instance, when measuring c in the SDW phase, as pictured in figure 2.2. Second, the behavior changes drastically between different system sizes. In this case, the Variance vs. V plots (not shown) for sizes 128 (blue "O") and 256 (green "+") have no local minimum to the left of V_{Gauss}, so that the flat sections of data in figure 2.3 are just the lowest V included in the data. In other words, variance increased monotonically from SDW through BOW before dipping at V_{Gauss} for these large domains. From a theoretical perspective, the methods' failure is obvious because curve fit 2.2 is lacking in corrections that appear at BKT points. Although we did pursue the additional logarithmic corrections (see future paper) for this project we found easier methods, described next.

2.3 Modified logarithmic derivative and central charge maximum for locating BKT transitions with open boundary conditions

In our search for a reliable and simple transition indicator at the BKT transition, we found an approach that is proven to work for ground states with periodic boundaries [47]. The method *depends on* the presence of a finite-size correction to central charge, c, at BKT points. This makes this method ideal for use with DMRG since DMRG is ideal for finite L. Adapting the method to OBC, as we do here, will make it even more useful, as DMRG converges best with OBC. In this section, we provide theoretical motivation for the method before developing an OBC version of the methods of [47]. In the results section we use these developments to study the EHM and successfully confirm the location of V_{BKT}.

The central charge in formula 2.4 has corrections at BKT transitions of the form $c = 1 + g^3$ where g is the coupling constant for a marginal operator [64]. This correction must be purely decreasing in the $L \to \infty$ limit (that is, along renormalization group flows) by Zamolodchikov's C-theorem [65], which implies conversely that as L decreases, c grows at BKT points. With this, we can now use our favorite method of extracting c to identify BKT transitions. The method developed here is the most convenient method available at the moment, since all that is needed is a set of OBC ground state wavefunctions.

For periodic boundaries, Ref. [47] started from equation 2.1 (with 6 replaced by 3) and took a derivative with respect to the logarithm, evaluated numerically close to the

chain midpoint. The result is an equation for the central charge:

$$c(x) = 3S_{vN}(x)\log\left(\frac{2L}{\pi}\sin\frac{\pi x}{L}\right) \tag{2.4}$$

which must be approximated for a discretized lattice by [47]

$$c(L/2) = 3\frac{S_{vN}(L/2-1) - S_{vN}(L/2)}{\log\cos\left(\frac{\pi}{L}\right)} \tag{2.5}$$

This simple form applies only when there is no oscillatory term, such that the numerical derivative can be evaluated on nearest neighbor bonds.

Since open boundaries, and higher Renyi index, will both induce oscillations in the entanglement [60], we propose to use the modified version based on equation 2.2, in which the finite differences are evaluated on next-nearest-neighbor sites (or n^{th}-order neighbors for longer, but still commensurate, wavelength oscillations) [32][3]. The result is

$$c(x) \equiv 6\frac{S_{vN}(x+1) - S_{vN}(x-1)}{\log\sin\left(\frac{\pi(x+1)}{L}\right) - \log\sin\left(\frac{\pi(x-1)}{L}\right)} \tag{2.6}$$

Two complications arise in this approach: first, even-numbered bonds produce different values of $c(x)$ than odd bonds, and second, equation 2.6 can behave poorly near $x = L/2$ due to inexact canceling of a 0 in the numerator and denominator.

We resolve the first difficulty by curve fitting $c_{even}(x)$ and $c_{odd}(x)$ separately, and then averaging the curve fits to produce a single function of x. We resolve the second difficulty by inspecting the data by eye to find aberrant values of $c(x)$ at the chain midpoint that we exclude from the curve fit. In practice, we cut out from 1 to 3 data points for every entropy dataset. The resulting curve, evaluated at $L/2$, provides our best estimate of c for a given system size L. This process is illustrated for entropy data in figure 2.7. This

[3]This was also used in reference [32] but for PBC

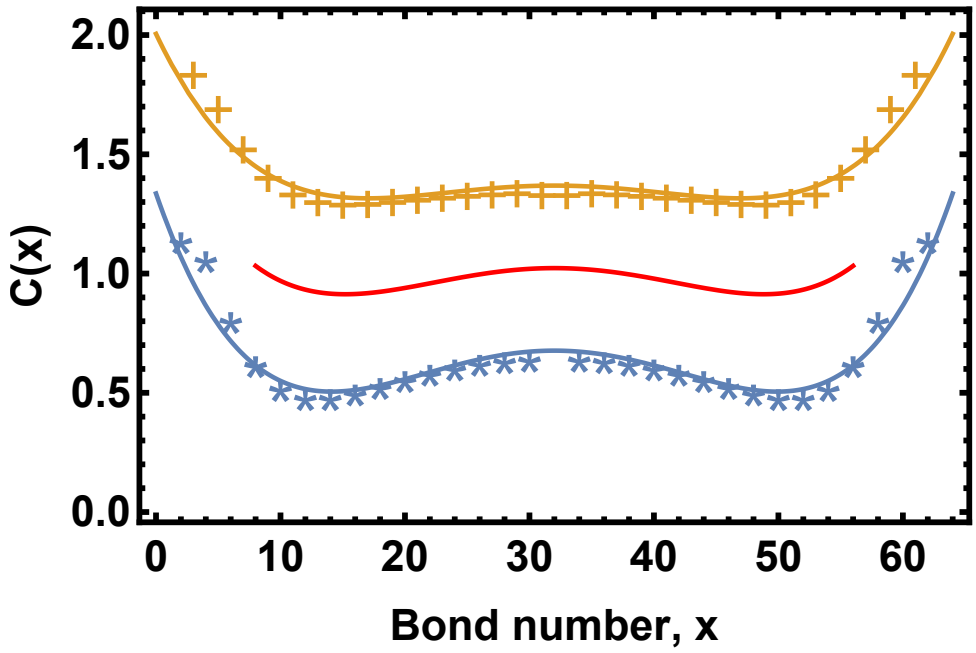

Figure 2.7: Numerical log-derivative method for central charge demonstrated for L = 64 at U = 4 and $V_{BKT} = 1.83$. The yellow pluses and yellow curve fit correspond to the even-bond log-derivatives while the blue stars and curve fit correspond to the odd-bond log-derivatives. Note that the midpoint blue star was removed due to a divergence. Red (middle) curve is the average of the yellow (upper) and blue (lower) curves. The "W" shape for c(x) is due to boundary effects; for larger L, c(x) flattens.

midpoint value of c(x) agrees well with the curve-fit scaling to the middle, implying that the two methods are complementary.

Lastly, as was done in Ref. [47], once we have $c(V)$ we used the maximum value to indicate the BKT transition. Of course, we can also use a regular curve fit (if desired, combined with scaling to the middle) to get $c(V)$. The methods we developed here for OBC likely require further refinement (see future publication). Although we did not use scaling in domain size (i.e. re-fit $c(x)$ for every possible domain of the data D) in combination with

the log-derivative approach, varying the domain D did provide an estimate of the error in c and the critical point, as reported in table 3.3.

Chapter 3

Results

In this section, we report our observations of the entropy for many system sizes. First, we study the unique form of the entropy at V_{Gauss} and present the result of our effort to identify that point using variance minimum in combination with scaling to the middle. This includes the observation of strange effects from a proposed charge soliton [1] that creates an effective bosonic degree of freedom at V_{Gauss}. Then we present the results of our study of V_{BKT} using both the log-derivative and curve fit methods before presenting our best estimate for V_{BKT}.

3.1 Second-order transition

First we summarize our efforts to identify V_{Gauss} using the combined variance minimum and scaling to the middle method, summarized in table 3.1.

[1] For a good introduction see [66]

Table 3.1: CFT curve fit results at the Gaussian critical point as determined by combining the *variance minimum* and *scaling to the middle* for equation 2.2. Observe that K increases with L, that S_0 and A are non-universal, and that A decays with L. The *numerical* resolution on V was 0.001 for all system sizes in this table. We report the estimated error in the last significant figure in parenthesis. The DMRG precision was limited by the values in **bold**; for small systems, M was unbounded, while for large systems, M was fixed. ΔE as reported here is a conservative estimate on the accuracy of the ground state energies achieved in our DMRG calculations. At V_{Gauss}, the soliton significantly increased entanglement, exceeding that at V_{BKT}, so that here only system sizes 16 and 32 are "exact" in the DMRG sense.

L	V_{Gauss}	S_0	**c**	A	$-K$	**M**	**trunc.**	**ΔE**
16	2.12 (2)	0.42(7)	2.0 (2)	0.25(NA)	0.04(NA)	900	**5E-14**	3E-12
32	2.150 (5)	0.30 (3)	2.12 (5)	0.18	0.12 (1)	2000	**5E-14**	3E-11
64	2.158 (1)	0.31 (1)	1.97 (1)	0.14	0.20 (1)	**3200**	1E-13	5E-9
128	2.1605 (5)	0.41 (5)	1.71 (5)	0.12	0.27 (2)	**3200**	1E-11	3E-7
256	2.160 (5)	0.65 (5)	1.4 (1)	0.10	0.29 (5)	**3200**	1E-10	3E-6

To quickly review how table 3.1 was produced, for each system size, and each domain, we identified a critical point from the minimum in the variance. Then, for each system size, we used "scaling to the middle" to get a best estimate of the critical point at an effective domain size of 0. This procedure is illustrated in figure 2.6.

One of the advantages of this approach is that it implicitly provides an error estimate for the measurements taken for a given system size. The errors we report in table 3.1 are estimated conservatively from the plot of a parameter versus fit domain or from the error in the constant term in the fit. For instance, for 64 sites, the procedure is illustrated in figure 2.6 which shows that the discretization of V, 0.001, is a good estimate of the error in the extrapolated value $V_{Gauss} = 2.158$.

Before discussing table 3.1 we look directly at a plot of the entanglement entropy as a function of cut position at V_{Gauss} in figure 3.1. The most obvious feature is that

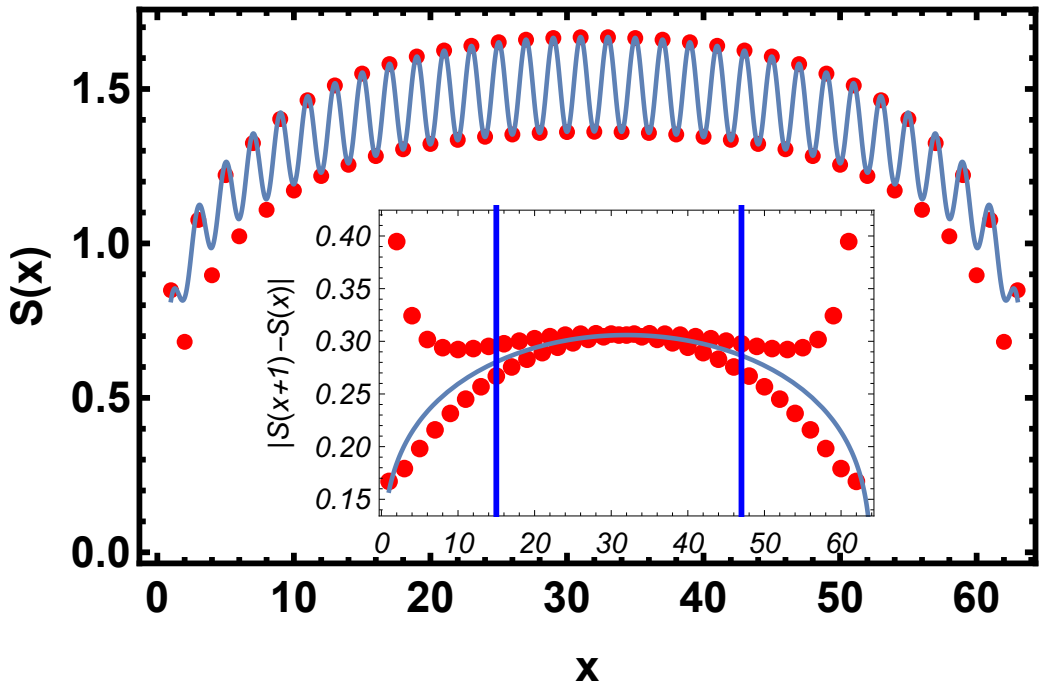

Figure 3.1: Main plot: entropy for 64 sites at $V_{Gauss} = 2.158$, and curve fit with D = 32. Inset: entanglement oscillation envelope. Also see figure 3.3.

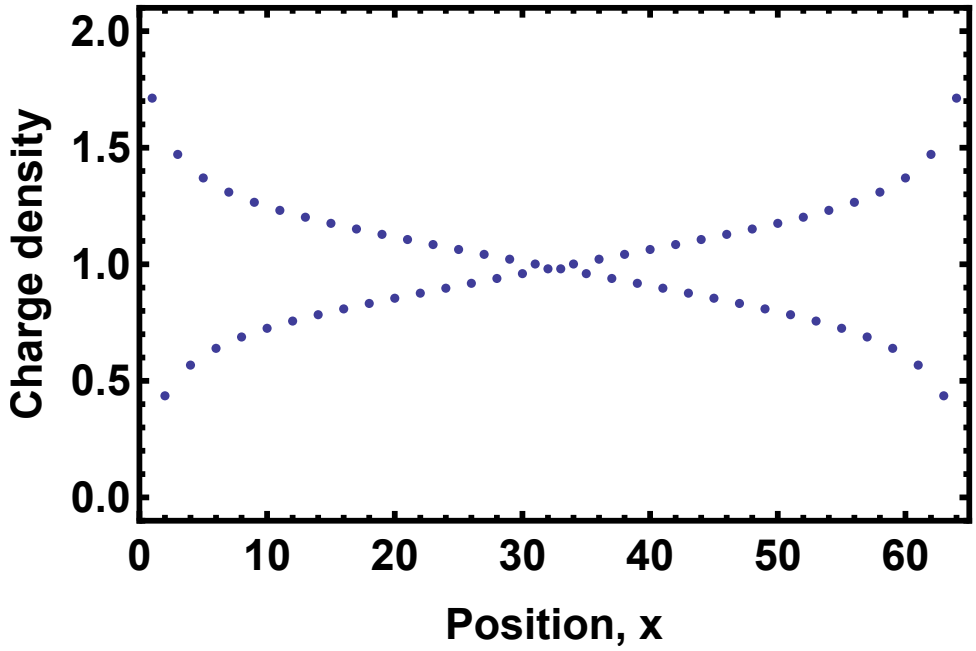

Figure 3.2: Charge density as a function of position at $V_{Gauss} = 2.158$ for 64 sites. Charge oscillations are distinct from the charge solition in figure 3.5, deep in the CDW phase.

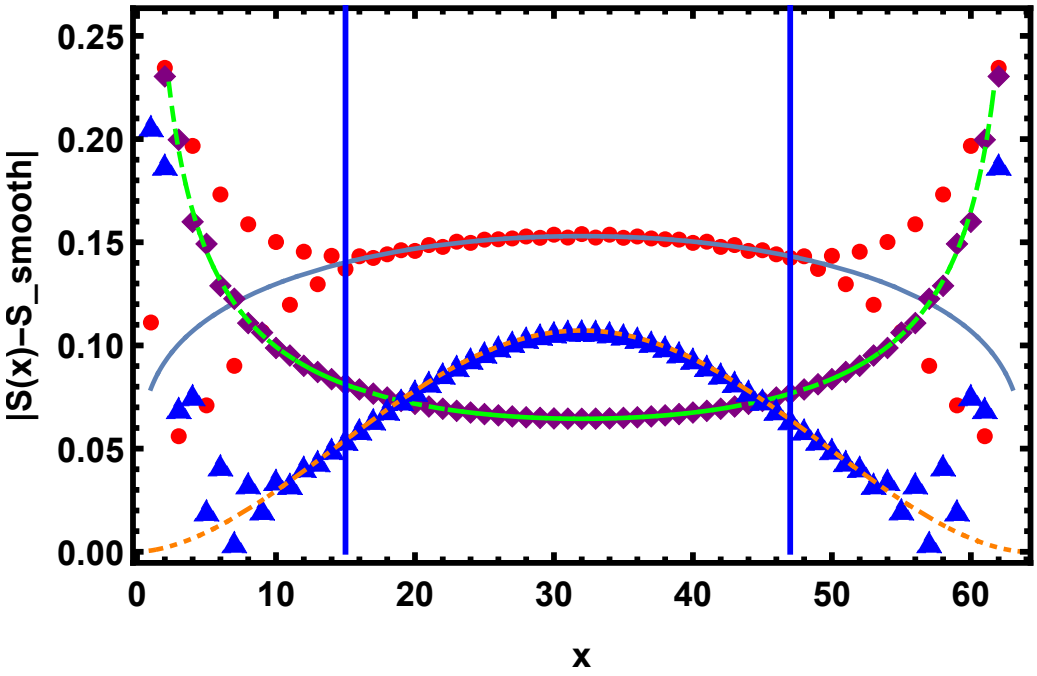

Figure 3.3: Entropy oscillation envelopes for V = 1 (SDW - purple diamonds and green dashes), $V_{Gauss} = 2.158$ (red dots and blue curve), V = 10 (CDW - blue triangles and orange dash-dot) for L = 64 sites. The SDW phase represents normal Luttinger Liquid behavior for comparison. For each plot, the data points were obtained by subtracting the best curve fit without the oscillatory component from the original entropy data. The smooth curves are the absolute value of the oscillatory component of the curve fit. At $V_{Gauss} = 2.158$, the envelope is a hybrid of the SDW and CDW envelopes. Curve fits were performed with D = 32 as indicated by blue vertical bars.

the oscillations don't decay away from the edges as expected at a critical point exhibiting Luttinger Liquid criticality [60]. The inset of figure 3.1 isolates this effect in an unbiased way, while figure 3.3 provides a curve-fit biased perspective. Compare figure 3.1 with figure 2.1 for a direct comparison of the entropy at V_{Gauss} and the SDW phase, which is a representative of normal Luttinger Liquid entropy.

Figure 3.3 is a plot of the raw entropy minus the smooth part of the CFT formula 2.1, fitted to the data for a middle-half domain. For completeness we include the oscillatory

part of the curve fit, $\frac{A(-1)^x}{(\sin\frac{\pi x}{L})^K}$, in the plot. There appears to be a competition between two separate effects at the Gaussian critical point; after about 16 sites in from the edge of the lattice, the expected decay of oscillations is overcome by a growth of oscillations.

This leads to a negative oscillation exponent (K in equation 2.2) for curve fit domains that exclude the 16 edge sites on either side of the chain. Since this growth of oscillations begins once the usual decay effects die down, we expect that decreasing the domain will improve the accuracy of the measurement of the value of the effective "K" that dominates on the interior of the lattice. Scaling to the middle is a good way to estimate this unexpected exponent. This assertion is supported by figure 3.3 and our experience fitting the data. If the edges are included in the curve fit, we found that the fit variance worsens drastically, because the two competing K values cancel each other.

As can be seen in table 3.1 the oscillation growth exponent of K increases with larger system sizes, showing that the soliton oscillation component is enhanced relative to the Friedel oscillation component when the system size is increased. On the other hand, the maximum oscillation amplitude A at the lattice midpoint (distinct from the amplitude at the edges) *does* decrease with increasing system size, just as the midpoint oscillation amplitude decreases with system size in a Luttinger Liquid. Table 3.1 also shows that central charge decreases from 2 with increasing system size (note that reference [67] measured c = 2.17 for L = 10 in the noninteracting case, U = V = 0). Although this statement is made with some caution, we also observed the central charge decreasing with scaling to the middle.

When we recognized that the oscillation growth could be due to a charge soliton, which is known to occur in the CDW phase, we studied the entropy in that region of the phase diagram (that is, $V > V_{Gauss}$) for comparison with our results at V_{Gauss}.

It turns out that the ground state energy is minimized in the CDW phase when two degenerate CDW's are present with a π phase shift. The entropy for this topological soliton defect, for OBC, is plotted in figure 3.4 and the density is plotted in figure 3.5. The entropy and density both fit well to combinations of sine functions as shown. In a brief side study on 16-site and 32-site lattices with PBC's, we found that the CDW phase has a uniform nonzero entanglement entropy due to the soliton/degeneracy effect. Comparing the envelopes of the entropy oscillatons in figure 3.3 for the CDW phase to V_{Gauss}, it seems plausible that the soliton is the cause of the growing oscillation envelope at the Gaussian point. With this knowledge, we can interpret the growth of oscillation amplitude as a result of combining the CFT scaling of equation 2.1 with the oscillation envelope in the curve fit used in figure 3.4. We did not pursue further linear combinations (or products) of sin() and 1/sin() to more accurately reflect the competing effects, but this might be useful to support a theoretical derivation of the entropy we observed.

To further confirm that the charge soliton was the source of the unexpected curve fit values for c and K, we tried various pinning configurations to select out one of the interfering degenerate ground states. For OBC, increasing the on-site energy U at site 1, while decreasing it at site L, is effective for this task and completely eliminates the soliton deep in the CDW phase as shown in figures 3.4 and 3.5. Likewise, for PBC, the nonzero entropy is lowered to 0 (i.e. a classical CDW) by increasing or decreasing U at a single site.

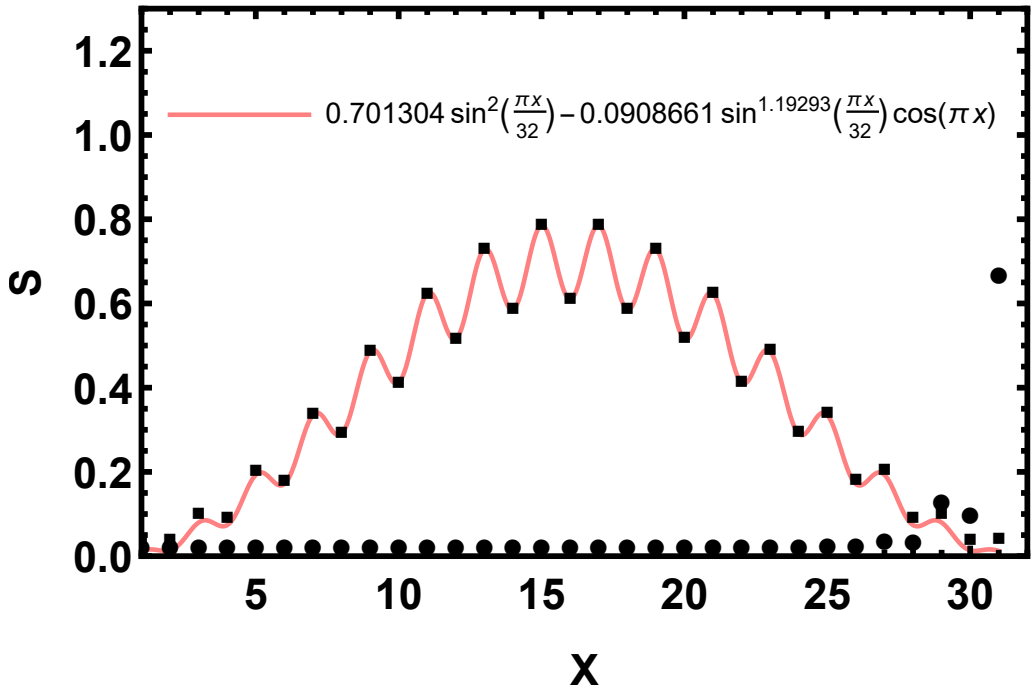

Figure 3.4: Entropy deep in the CDW phase fits well to a combination of sine functions, as shown here for 32 sites at U = 4 and V = 10 with OBC. The square points show the entropy without pinning, while the round points show a reduction in entropy with pinning. Here U = U + 1.0 at the left edge and U = U - 1.0 at the right edge.

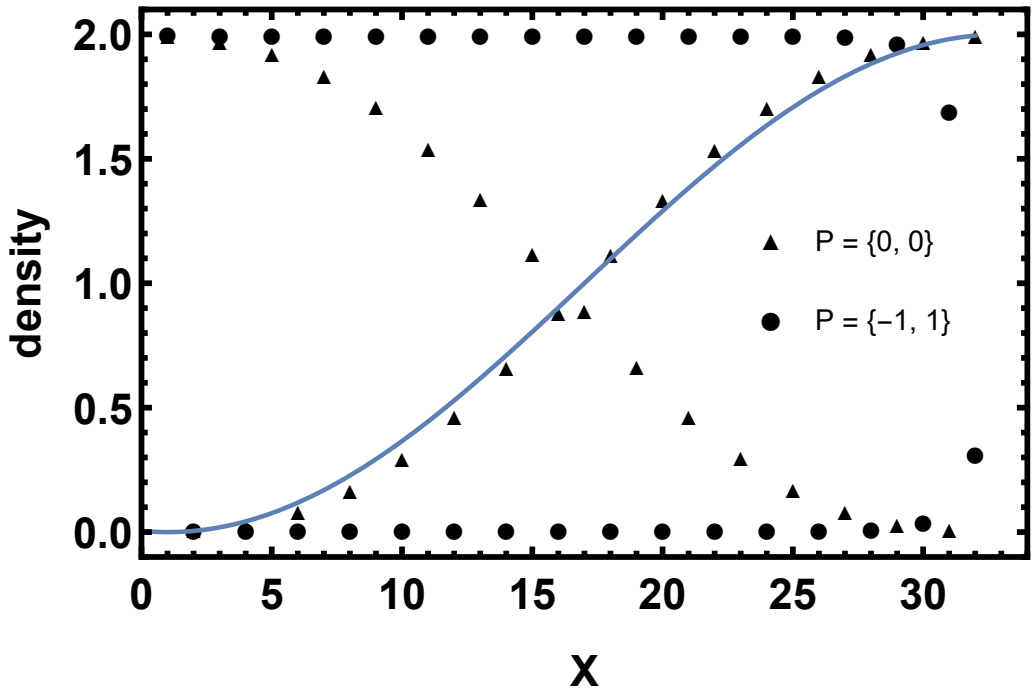

Figure 3.5: Charge density for N = 32 sites, U = 4, V = 10, deep in the CDW phase with and without pinned edges. Pinning takes the form U + P where P is 0 or ± 1 at the edges and eliminates a topological defect (a kink-soliton). The envelope of the density fits approximately to 2 $\sin\left(\frac{\pi(x-1)}{2L}\right)^2$ as shown as a blue curve.

Next we attempted a similar program of edge pinning at V_{Gauss} to eliminate the increased value of c and negative K. With fine-tuned pinning, in this case with additional *positive U at both site 1 and site L*, we were able to recover both a central charge close to 1 (best result was 1.2 for 64 sites) and regular Luttinger Liquid effects (K was about 0.5 for 64 sites, close to the previous Monte Carlo best estimate of 0.44) [33]. This particular arrangement of fine-tuned pinning softens the boundary conditions and reduces the soliton, hinting at further work to be explored with alternative boundary conditions [68] applied to this model, which may combine nicely with "scaling to the middle" to extract accurate infinite-size values.

The growth of the entropy oscillations we present in figure 3.4 and table 3.1 was also displayed in Ref. [69] in a different model with charge oscillations, however the authors did not investigate the growth of the oscillations from the open boundaries.

We briefly studied a 16-site lattice at V_{Gauss} with PBC. Although the entropy oscillations went away, we still found an increased central charge of 2, which further supports the presence of a soliton for finite-sized chains at this critical point. In the CDW phase ($V > V_{Gauss}$), for periodic boundaries, the soliton was eliminated easily by increasing U at a single site. This strategy worked at V_{Gauss} as well, bringing the central charge down to the thermodynamic-limit value of 1, while inducing a small charge oscillation. From these observations, we propose that the soliton is contributing a second bosonic degree of freedom for small systems, and that this effect should have experimental consequences.

For open boundary conditions, we can see from our data in table 3.1 that the central charge of 2, and hence the soliton, is largely unchanged until the system size reaches

about 100 sites. This is encapsulated by the approximate scaling of c with L, according to the function $c(L) \approx 1 + \tanh(100/L)$. To arrive at this function, we included preliminary calculations of large (512 and 1024) sizes; these also showed oscillation growth from the boundaries. However, our data was incomplete and had large truncation errors relative to our other sizes, so we chose to hold back on reporting these results, as promising as they were [2]. Our evidence that c decreases to 1 as system size increases could conceivably be a finite-entanglement effect, since our larger system calculations come with entropy loss (in other words, more truncation error). These size vs entanglement scaling effects can be subtle [41] and would require additional effort to resolve unambiguously. As mentioned previously, scaling to the middle also supports the observation that c decreases to 1.

3.2 BKT transition

It has been known for some time that BKT transitions are difficult to detect numerically due to the slow closing of the gap for standard order-parameter and energy gap methods [33]. Previous entanglement entropy studies of the EHM's BKT transition have been imprecise: using the two-site and block entropies leads to a discrepancy in V_{BKT} of about 0.1 from the best published results, even though the system sizes were large (512 sites) and the truncation error low (equivalently, high bond dimension M = 3000) [46]. We identified an approach that provides a sharper, more accurate transition indicator, based on the universal scaling law (2.2) for the ground-state entanglement.

[2] In order to accurately study the critical behavior, we need to first find the critical point precisely. Since the critical point sharpens as system size increases, and since computational cost grows rapidly with system size, the necessary scan across many V values is very computationally demanding.

Table 3.2: Critical point and resulting curve fit parameters as determined by fitting the entanglement entropy, equation 2.2, and applying the "scaling to the middle" approach for all parameters to reduce boundary effects. The maximum in $c(V)$ was used to identify the critical point. A, defined in the text, is a measure of the amplitude of the oscillatory component of the entropy. This approach failed for 16 sites, but the log-derivative method did work for 16 sites, table 3.3. K = 1/2 matches expectations for the Heisenberg model. For sizes 16 and 32, we did not record the maximum bond dimensions. The bolded values were used to set the DMRG convergence. When the truncation error (trunc) was used, M was allowed to grow unbounded; when M was fixed (due to resource limitations) sweeps were continued until ΔE or trunc was achieved.

L	V_{BKT}	S_0	**c**	A	**K**	**M**	**trunc**	**ΔE**
16	NA	NA	NA	NA	NA	NA	**1E-13**	1E-12
32	1.56 (1)	0.776 (5)	0.974 (5)	0.12 (1)	0.5965 (3)	NA	**1E-13**	1E-12
64	1.82 (1)	0.76 (1)	1.0542 (2)	0.10 (1)	0.563 (3)	2000	**5E-14**	5E-10
128	1.95 (1)	0.780 (5)	1.060 (1)	0.08 (1)	0.492 (9)	**3200**	1E-12	2E-8
256	1.93 (1)	0.797 (1)	1.028 (1)	0.06 (1)	0.4862 (2)	**3200**	1E-11	1E-7

As shown in Ref. [47] and citations to that article [70–73], the peak in the central charge provides a reliable, universal way of identifying BKT transitions from finite-size data. We demonstrate this approach for the EHM, with two methods: 1) extracting the central charge for each V with a simple curve fit that has been scaled to the middle, and 2) using the logarithmic derivative method to extract central charge for each V, as described in the Methods section, 2.3. The results presented below are to be compared against the most reliable, found in Refs. [3, 33] which relied on finite-size scaling of up to 1000 sites; for U = 4, $V_{BKT} = 1.877$ by DMRG, and $V_{BKT} = 1.89(1)$ by QMC, respectively.

The most obvious way to identify the central charge, and hence the peak, is with a regular curve fit; we also apply scaling to the middle for further gains in precision. The values of $c(V)_{max}$ extracted this way are shown in table 3.2. One advantage of this approach is that all of the curve-fit parameters can be tabulated, including the Luttinger exponent K and the constant term in the entropy. As a result, as shown in table 3.2, we found that the

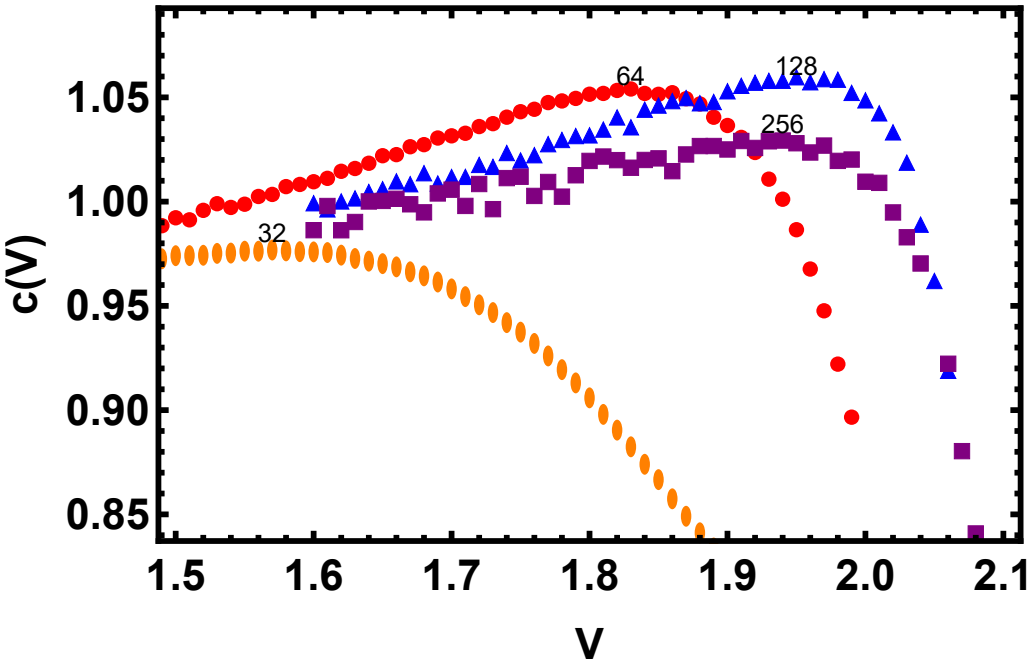

Figure 3.6: Plot of c(V) for all system sizes from log-derivative method. 32 sites has orange ellipses, 64 sites has red circles, 128 sites has blue triangles, and 256 sites has purple rectangles. Up to L = 128, c_{max} and V_{max} increase with L, before decreasing from L = 128 to 256.

constant term in the entropy, S_0, is size-independent [3]. The disadvantage of this approach is that about 32 sites are required to use scaling to the middle. This implies, for instance, that if the cold atoms under study are in a symmetric confining potential (for instance $U(x) \approx U + \Delta U x^2$), then nearly 32 atoms are needed to use scaling to the middle.

The results of the second way of extracting $c(V)_{max}$ that we tested, as adapted from Ref. [47], are presented in table 3.3 and figure 3.6. These results agree very well with the regular curve-fit method reported in table 3.2 and described above. This method has

[3] Nishimoto [47] did not study the constant term at BKT transitions because his log-derivative approach removes it.

the advantage, over curve-fitting, that fewer sites are needed to extract the critical point, providing easy access for experiments.

Here we discuss figure 3.6 and put it into context. First, this figure corresponds to figure 1 in Ref. [47], which shows analogous plots of $c(J_2/J_1)$ for the J_1-J_2 model with periodic boundary conditions near a BKT point. There, three main observations are made: "c_{max}" decreases with increasing system size; the critical coupling, $(J_2/J_1)_{max}$, decreases with increasing system size; and in the infinite size limit, $c(J_2/J_1)$ approximates a unit step function (c takes the value 1 in the critical phase and drops off in the gapped phase). The sizes presented were 32, 64, 96, and 128. In our figure 3.6 and table 3.3, we find the opposite trend for sizes 16 (not plotted), 32, and 64 sites; we see c_{max} increases, and V_{max} increases, as L increases. Then, this trend reverses, and for 128 and 256 sites, both c_{max} and V_{max} decrease. We see the step function behavior, as c is nearly 1 in the SDW phase before peaking at the BKT transition and then dropping sharply in the BOW phase.

This more complicated behavior has two apparent causes. First, the BKT point is not immune to the CDW effects studied at V_{Gauss}. As revealed in the previous section, we expect those effects to dominate up to system sizes about 100 sites, but also to push the effective critical point to lower V (as seen here) as the CDW survives at the boundaries and breaks the symmetry of the critical point. In this way, the BKT point has CDW boundary effects that decay with system size up to about 100 sites. The second cause could be the worse truncation errors for larger systems, which could account for both the scatter in the data as well as the decrease in c. We tested this hypothesis by recreating the plots with bond dimension M decreased from 3200 to 1600, and observed no changes in the locations of

the peaks for any of the sizes presented. With this accuracy check, we can safely state that the behavior is a real finite-size effect, and that our larger L = 128 and 256 are exhibiting the finite-size behavior shown in fig. 1 of Ref. [47]. Future studies of this BKT point should avoid sizes below L = 100. Since L = 128 and 256 have reached the scaling regime, we feel confident claiming $V_{BKT} < 1.94$ in the infinite-size limit (or 1.93 from table 3.2).

Now we may also resolve the issue of the apparent scatter in the plots for larger L in figure 3.6, which is not due to DMRG, but rather the log-derivative. For larger systems, S(x) data near the lattice midpoint is very flat, which introduces extreme sensitivity in the numerical log-derivative. This scatter in the data in figure 3.6 leads to larger error estimates in table 3.3. However, with refinement of the method, the scatter could be reduced.

Table 3.3: The BKT point, determined by finding a maximum in central charge c as a function of V, which was computed with the modified logarithmic derivative method. Raw data is plotted in figure 3.6.

L	V_{BKT}^{mid}	c_{BKT}^{mid}
16	1.29(2)	0.89(1)
32	1.57(3)	0.975(2)
64	1.83(3)	1.052(2)
128	1.95(2)	1.058(2)
256	1.94(2)	1.027(2)

We conclude this section by making our final and best estimate of the critical point, V_{BKT}, based on the c-max method. As done in Ref. [47] (see figure 2), we can linearly fit V_{max} vs 1/L and extrapolate to 1/L = 0 to get V_{BKT}. For 128 and 256 sites, using the data from Table 3.2, this yields $V_{BKT} = 1.91(3)$. The error of 0.03 was estimated by re-fitting the line at the bounds of V_{BKT}. As a range, we find that $1.88 < V_{BKT} < 1.94$, in agreement with previous publications and in support of $V_{BKT} < U/2$.

Chapter 4

Conclusions, Acknowledgements, and Follow-Up Work

4.1 Conclusions

We have successfully demonstrated the identification of quantum critical points for the Extended Hubbard Model in 1D for both the second-order and the Berezinskii-Kosterlitz-Thouless transitions using nothing but the ground state von-Neumann entanglement entropy and results from Conformal Field Theory. Along the way we have introduced two refined methods for resolving quantum phase diagrams: "Scaling to the Middle" which provides improved measurement accuracy of any spatial curve fit on open boundary data, and an extended log-derivative approach for the study of central charge from open boundary data. Since the central charge exhibits a finite-size-effect peak at BKT transitions, it

can then be used to identify such transitions from experimentally realistic system sizes. In combination with a CFT-fitted variance minimum, these tools enable reliable small-scale studies of numerical and experimental (i.e. cold-atom) entropy data.

In addition, we have identified the role played by soliton physics at the Gaussian critical point in the Extended Hubbard Model at half-filling; namely, it leads to an additional bosonic degree of freedom that appears as an addition to the central charge for systems up to about 100 sites in length. This same soliton effect is also responsible for entanglement entropy oscillations that grow, rather than decay, from open boundaries, in contrast to the expected Luttinger Liquid oscillations.

4.2 Acknowledgements

We thank John Cardy for helpful contributions to our studies of the BKT transition (also see forthcoming publication) and Miles Stoudenmire for extensive discussions on ITensor. This research was supported in part by the NSF under grant DMR-1411345 and by UCR's GRMP fellowship. This work used the Extreme Science and Engineering Discovery Environment (XSEDE) COMET at the San Diego Supercomputer Center through allocation TG-DMR170082 [74].

4.3 Follow-Up Work

Since the publication of this work in 2019, additional work was completed to add to the study of the observations reported here.

Part II

Analytical Study of Extended Hubbard Model with Disorder

Chapter 5

Analysis and model translations

In this chapter, I present the main theoretical task required to solve the second problem. Starting from the Hamiltonian of the extended Hubbard model with disorder, derive a renormalization group flow that can reveal the correct low-energy physics.

Thanks to the long history of studies of the extended Hubbard model, work has been done on this problem. What follows is essentially an attempt to merge the analyses of two authors: T+F who studied the U-V model and showed that the BOW phase can be detected using a weak-coupling analysis. This was done by including high-energy corrections in g-ology coefficients, and when $U \approxeq 2V$, these corrections lead to breaking an accidental symmetry (while inducing the coefficients for the spin sector theory to become negative). F+K showed that for the U-Δ model, there is a transition between a Mott insulator and an Anderson insulator. T+F provides the necessary high energy corrected g-ology coefficients which are then input into the RG flows determined by F+K for the EHM with disorder. For

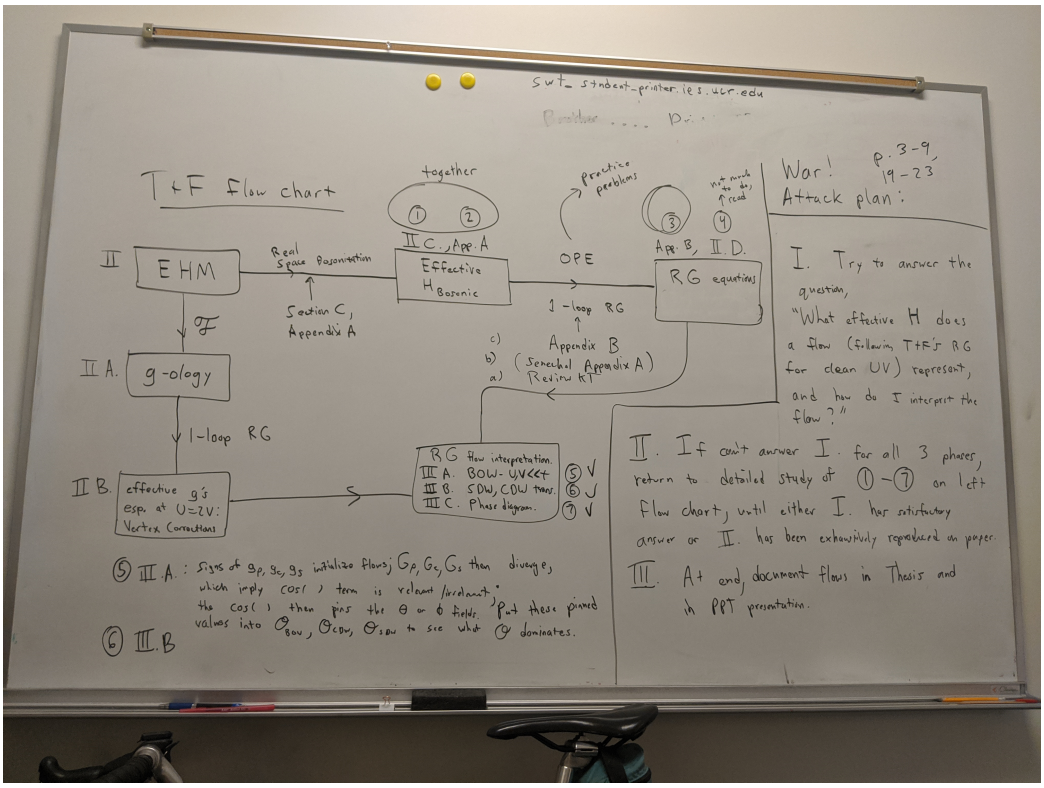

Figure 5.1: The needed steps to follow T+F's derivation of the BOW phase diagram.

me to perform this merger and have confidence in the resulting RG flow equations, I found it was necessary to repeat for myself as much of T+F and F+K's derivations as possible, as well as test and compare the resulting RG flows in the parameter regimes that match.

Having a lack of experience in this subject, I created the flow chart in figure 5.1 to chart a course to understanding T+F's paper; the flow chart helped me decide which parts to focus on in detail and which parts to skim and in what order. This then prepares me to derive F+K's flow equations. A similar diagram is provided in the next figure 5.2 below, roughly outlining how to complete the derivation of F+K's flows.

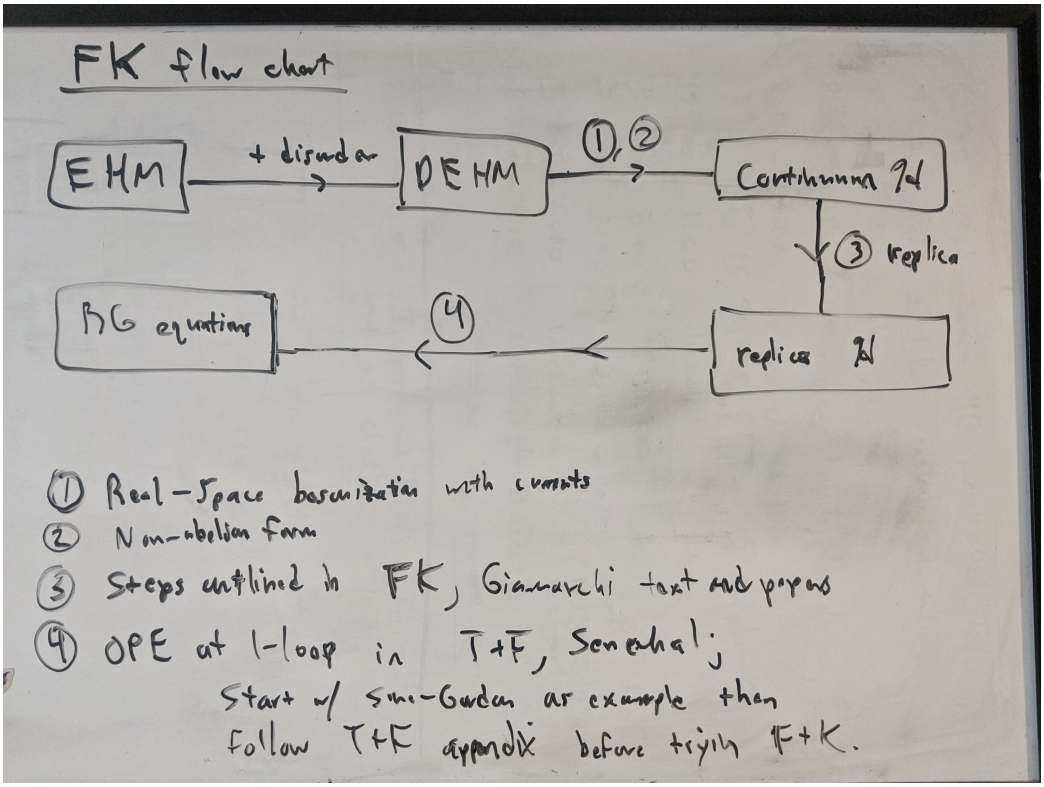

Figure 5.2: The needed steps to follow F+K's derivation of the disordered Hubbard model flow equations.

To begin with, T+F provides an abelian bosonization analysis of their g-ology coefficients. I start in the first section by ensuring that our choice of notation is consistent with T+F's definitions, as well as Nakamura (similar to Giamarchi text). I derive RG equations for the clean model in this notation.

In the second section, I re-derive the bosonized hamiltonian following conventions from Senechal's review article. This requires careful comparison to get signs correct. Senechal's notation, in terms of currents, provides a quick path to non-abelian bosonization. This is convenient for comparison with F+K's methods and RG equations.

Lastly, in the third section, I add a disorder term to the original model in real-space. I bosonize that in non-abelian notation, with help from Senechal. Then I derive final RG equations to compare with F+K's RG equations.

It was important to match the different sign conventions and have "sanity checks" to compare my RG flows with prior publication results, as well as get a sense for what the simpler flows are telling us before attempting to interpret the full disordered system flows.

5.1 Consistent notation: Clean Case, Abelian

One of the primary challenges of this project is translating notation from multiple authors and combining it into the model we are studying. In this section I document the notation that I use for constructing the clean, abelian, bosonic model from which the BOW

RG flows can be derived. The Hamiltonian is

$$\begin{aligned} H &= -t\sum_{\sigma}\sum_{i=1}^{L}(c^{\dagger}_{i+1,\sigma}c_{i,\sigma} + H.c.) + U\sum_{i=1}^{L} n_{i,\uparrow}n_{i,\downarrow} \\ &\quad + V\sum_{i=1}^{L} n_i n_{i+1}, \end{aligned} \tag{5.1}$$

.

I start at [75] equation 6, the Bosonic version of 5.1, with $\delta = 0$ and $q = 1$ at half filling. By defining $\Pi_\nu = \frac{1}{\pi}\partial_x\theta_\nu$ we arrive at notation consistent with Giamarchi's appendix D [76],

$$\begin{aligned} \mathcal{H}_{clean} &= \sum_{\nu=\rho,\sigma}\frac{v_\nu}{2\pi}\int dx[K_\nu\left(\pi\Pi_\nu(x)\right)^2 + \frac{1}{K_\nu}\partial_x\phi_\nu(x)^2] \\ &\quad + \frac{2g_{1\perp}}{(2\pi\alpha)^2}\cos(\sqrt{8}\phi_\sigma(x)) \\ &\quad + \frac{2g_{3\perp}}{(2\pi\alpha)^2}\cos(\sqrt{8}\phi_\rho(x)) \\ &\quad + \frac{2g_{3\parallel}}{(2\pi\alpha)^2}\cos(\sqrt{8}\phi_\rho(x))\cos(\sqrt{8}\phi_\sigma(x)). \end{aligned} \tag{5.2}$$

This form for the momentum is nice because it leads to a canonical commutator $[\phi(x), \Pi(x')] = i\delta(x - x')$. The reference [77] defines both the Lagrangian (Hamiltonian) without any factors of π and the canonical momentum with a relative factor of $-\pi$, but this won't concern us here.

The bosonic constants, K_ρ, v_ρ, K_σ, and v_σ, can be derived by substituting the fermion to boson mapping. The appendix in [75] provides these (equation A1) but leaves

out the definitions of the g's. The relationships provided by [75] are

$$\begin{aligned} v_\nu &= \sqrt{u_\nu^2 - \left(\frac{g_\nu}{2\pi}\right)^2} \\ K_\nu &= \sqrt{\frac{2\pi u_\nu + g_\nu}{2\pi u_\nu - g_\nu}} \\ u_\nu &\equiv v_F + \frac{g_{4\parallel} \pm g_{4\perp}}{2\pi} \\ g_\nu &\equiv g_{1\parallel} - g_{2\parallel} \mp g_{2\perp} \\ g_{1,\perp} &= g_\sigma \end{aligned} \tag{5.3}$$

where the upper and lower sign is for charge, ρ and spin, σ fields, respectively. The paper [75] builds off of the notation in [78] and so we continue with that notation here.

For convenience I list the above formulas with the bare g-ology substituted, but not yet in terms of U and V:

$$\begin{aligned} v_\sigma &= \sqrt{\left(v_f + \frac{g_{4\parallel} - g_{4\perp}}{2\pi}\right)^2 - \left(\frac{g_{1\parallel} - g_{2\parallel} + g_{2\perp}}{2\pi}\right)^2} \\ K_\sigma &= \sqrt{\frac{2\pi v_f + g_{4\parallel} - g_{4\perp} + g_{1\parallel} - g_{2\parallel} + g_{2\perp}}{2\pi v_f + g_{4\parallel} - g_{4\perp} - g_{1\parallel} + g_{2\parallel} - g_{2\perp}}} \\ v_\rho &= \sqrt{\left(v_f + \frac{g_{4\parallel} + g_{4\perp}}{2\pi}\right)^2 - \left(\frac{g_{1\parallel} - g_{2\parallel} - g_{2\perp}}{2\pi}\right)^2} \\ K_\rho &= \sqrt{\frac{2\pi v_f + g_{4\parallel} + g_{4\perp} + g_{1\parallel} - g_{2\parallel} - g_{2\perp}}{2\pi v_f + g_{4\parallel} + g_{4\perp} - g_{1\parallel} + g_{2\parallel} + g_{2\perp}}} \end{aligned} \tag{5.4}$$

We also list the definitions of the g's from [78], repeated below, consistent with the notation in [75] used above:

$$\begin{aligned} g_{1\perp} &= U - 2V \\ g_{1\parallel} &= -2V \\ g_{2\perp} &= U + 2V \\ g_{2\parallel} &= 2V \\ g_{3\perp} &= U - 2V \\ g_{3\parallel} &= -2V \\ g_{4\perp} &= U + 2V \\ g_{4\parallel} &= 2V \end{aligned} \tag{5.5}$$

With these definitions substituted into 5.3, the coefficients become

$$\begin{aligned} K_\rho &= \sqrt{\frac{\pi v_f - V}{\pi v_f + U + 5V}}, \\ v_\rho &= \sqrt{v_f^2 + \frac{(U+4V)v_f}{\pi} - \frac{V(U+5V)}{\pi^2}}, \\ K_\sigma &= \sqrt{\frac{\pi v_f - V}{\pi v_f - U + V}}, \\ v_\sigma &= \sqrt{v_f^2 - \frac{v_f U}{\pi} + \frac{V(U-V)}{\pi^2}}. \end{aligned} \tag{5.6}$$

Note that $g_{1\perp}$ and $g_{3\perp}$ do not enter into these parameters at all. They only appear in the symmetry breaking cosine terms in the Hamiltonian.

This bosonic model and set of coefficients will not lead to a BOW phase unless corrected $g_{1,\perp}$ and $g_{3,\perp}$ are incorporated into equations 5.5 as explained in [79]. I repeat

these crucial corrections here:

$$\begin{aligned} g_{1\perp} &= (U-2V)\left[1-\frac{C_1}{4\pi}(U-2V)\right]-\frac{C_2V^2}{\pi} \\ g_{3\perp} &= (U-2V)\left[1+\frac{C_1}{4\pi}(U+6V)\right]+\frac{C_2V^2}{\pi} \\ C_1(\Lambda) &\equiv 2\ln(\cot(\Lambda/2)) \\ C_2(\Lambda) &\equiv 2\cos(\Lambda). \end{aligned} \tag{5.7}$$

With these corrections, we can quickly understand the (mathematical) source of the BOW phase when U = 2V. Looking at equations 5.2, the symmetry breaking cosine terms will have a coefficient of 0 when $U = 2V$. This line was previously thought to be a single phase transition. However, with the corrections, the cosine for the charge field has a positive coefficient when $U = 2V$, and the cosine for the spin field has a negative coefficient when $U = 2V$. In a mean-field sense, the symmetry breaking for the spin field will favor values $n\pi$ while the charge field will favor $(2n+1)\pi/2$ close to $U = 2V$. I review this later in the notation of [79] in section 6.1, where I also reproduce the clean BOW weak-coupling phase diagram as practice.

5.2 Consistent notation: Disorder added to Abelian model

I add the following on-site disorder,

$$H_{dis} = \sum_{i=1}^{L}\epsilon_i n_i \tag{5.8}$$

$$= \sum_{i=1}^{L}\sum_{\sigma=\uparrow,\downarrow}\epsilon_i(c^\dagger_{i,\sigma}c_{i,\sigma}) \tag{5.9}$$

to the hamiltonian 5.1, with the gaussian-distributed disorder ϵ_i that is compatible with a replica trick.

I re-emphasize that the purpose of this section is to provide notational continuity to avoid errors. To that end, notice there is a sign conflict between two of our references for the disorder contribution to the bosonic model; compare equation 9.29 in [76], which has a (-) on the forward-scattering disorder term, to equation 4 in [80] which lacks this sign.

What is the origin of this sign difference, and will it affect our eventual RG flows? The answer to the latter question is no, because performing a replica trick will square any coefficients on the disorder to treat it as a source of fluctuations. So we won't waste time worrying about the source of the sign difference.

Sticking with [76] notation, we have

$$H_{dis} = - \frac{\sqrt{2}}{\pi} \int_0^L dx \eta(x) \nabla \phi_\rho(x) \tag{5.10}$$

$$+ \frac{1}{2\pi\alpha} \int_0^L dx \xi^*(x) e^{i\sqrt{2}\phi_\rho(x)} \cos\left(\sqrt{2}\phi_\sigma(x)\right) + h.c. \tag{5.11}$$

One difference between [76] and [80] is that [76] implicitly includes the $+2k_f$ scattering in the definition of the backscattering amplitude (see equation 9.22 [76]).

5.3 Consistent notation: Clean, Non-Abelian spin sector

In this section, we systematically derive the non-abelian spin Hamiltonian, equation 3 in [80], from equations 5.2 above. This is a useful exercise for purposes of translating between the two forms of the Hamiltonian which we then need for use in the flow equations.

Repeating here the spin-sector components of equations 5.2,

$$\begin{aligned}\mathcal{H}_{clean} &= \frac{v_\sigma}{2\pi}\int dx[K_\sigma\left(\pi\Pi_\sigma(x)\right)^2+\frac{1}{K_\sigma}\partial_x\phi_\sigma(x)^2] \\ &+\frac{2g_{1\perp}}{(2\pi\alpha)^2}\cos(\sqrt{8}\phi_\sigma(x)) \\ &+\frac{2g_{3\|}}{(2\pi\alpha)^2}\cos(\sqrt{8}\phi_\rho(x))\cos(\sqrt{8}\phi_\sigma(x)).\end{aligned} \tag{5.12}$$

Now, we'd like to rewrite this in terms of SU(2) invariant currents. Although this translation is simple in principle, it is complicated by the task of translating between different authors' definitions of the bosonic model. At this point, a messy accounting job is required that bridges the gaps left by several sets of equivalent notation.

1.

Write down Senechal's hamiltonian in terms of currents (including interactions). Then translate back into bosonic form; compare with equations 5.2 above.

$$\begin{aligned}H_s &= \frac{2\pi v+2vg_{4,s}}{3}[\vec{J_L}(x)\cdot\vec{J_L}(x)+\vec{J_R}(x)\cdot\vec{J_R}(x)] \\ &+ -2vg_1\left(J_R^xJ_L^x+J_R^yJ_L^y\right) \\ &+ 4vg_{2,s}J_R^zJ_L^z\end{aligned} \tag{5.13}$$

We apply $g_1=-2g_{2,s}$ which is for now in the notation of [77], we write this as

$$\begin{aligned}H_s &= \frac{2\pi v+2vg_{4,s}}{3}[\vec{J_L}(x)\cdot\vec{J_L}(x)+\vec{J_R}(x)\cdot\vec{J_R}(x)] \\ &- 2vg_1\left(J_R^xJ_L^x+J_R^yJ_L^y+J_R^zJ_L^z\right)\end{aligned} \tag{5.14}$$

This can be re-written as

$$\begin{aligned}H_s &= \frac{2\pi v+2vg_{4,s}}{3}[\vec{J_L}(x)\cdot\vec{J_L}(x)+\vec{J_R}(x)\cdot\vec{J_R}(x)] \\ &- 2vg_1\vec{J_R}(x)\cdot\vec{J_L}(x)\end{aligned} \tag{5.15}$$

Next I apply Senechal's equations 7.1 for the right-moving currents. (although first I derived the forms of the left-moving currents.) The components of the spin currents are derived by substituting the bosonization formulas for the spinful fermion fields, and I don't show the uninteresting details. Since the currents with opposite chirality commute we don't need point splitting to get these.

First, the right-moving z component is

$$J_z^R = \frac{i}{\sqrt{2\pi}}\partial_z\varphi_s(x) \tag{5.16}$$

and the left-moving component is

$$J_z^L = \frac{-i}{\sqrt{2\pi}}\partial_{\bar{z}}\varphi_s(x) \tag{5.17}$$

where the partial derivatives are defined in [77] equations 2.4, with respect to $z = -i(x - vt)$ and $\bar{z} = i(x + vt)$ respectively, and $\varphi(x) = \phi_L(\bar{z}) + \phi_R(z)$ is a sum of left and right moving bosonic spin fields.

For the x components of the current I find

$$J_x^R = \frac{i}{2\pi}\eta_\uparrow\eta_\downarrow \sin\left(\sqrt{8\pi}\phi_R\right) \tag{5.18}$$

$$J_x^L = \frac{-i}{2\pi}\bar{\eta}_\uparrow\bar{\eta}_\downarrow \sin\left(\sqrt{8\pi}\phi_L\right) \tag{5.19}$$

and finally for the y components I get

$$J_y^R = \frac{-i}{2\pi}\eta_\uparrow\eta_\downarrow \cos\left(\sqrt{8\pi}\phi_R\right) \tag{5.20}$$

$$J_y^L = \frac{-i}{2\pi}\bar{\eta}_\uparrow\bar{\eta}_\downarrow \cos\left(\sqrt{8\pi}\phi_L\right) \tag{5.21}$$

in which η_σ ensures fermionic statistics.

After substituting these into H_s above, I get

$$\begin{aligned} H_s &= \frac{2v + 2vg_{4,s}}{3}[\vec{J_L}(x) \cdot \vec{J_L}(x) + \vec{J_R}(x) \cdot \vec{J_R}(x)] \\ &\quad -2vg_1 \left(\frac{-1}{(2\pi)^2} \cos\left(\sqrt{8\pi}\varphi_s(x)\right) + \frac{1}{2\pi}\partial_z\varphi_s(x)\partial_{\bar{z}}\varphi_s(x) \right) \end{aligned} \tag{5.22}$$

The first term comes from [77] equation 6.64, yielding

$$\begin{aligned} H_s &= -(v + \frac{vg_{4,s}}{\pi})[(\partial_z\varphi_s(x))^2 + (\partial_{\bar{z}}\varphi_s(x))^2] \\ &\quad -2vg_1 \left(\frac{-1}{(2\pi)^2} \cos\left(\sqrt{8\pi}\varphi\right) + \frac{1}{2\pi}\partial_z\varphi_s(x)\partial_{\bar{z}}\varphi_s(x) \right). \end{aligned} \tag{5.23}$$

By completing the conversion to real-space and time coordinates (using [77] equations 2.4), we should return ourselves to the original sine-gordon luttinger model with cosine term given in [77] eq. 5.60 and luttinger coefficients defined for the hamiltonian in [77] eq.s 6.4 and 6.5. I do so by first putting the above derivative terms into real-space,

$$\begin{aligned} H_s &= \left(\frac{v}{2} + \frac{vg_{4,s}}{2\pi}\right)[(\partial_t\varphi_s(x)/v)^2 + (\partial_x\varphi_s(x))^2] \\ &+ \frac{vg_1}{2\pi}\left(\frac{1}{\pi}\cos\left(\sqrt{8\pi}\varphi_s(x)\right) + \frac{1}{2}\left((\partial_t\varphi_s(x)/v)^2 - (\partial_x\varphi_s(x))^2\right) \right) \end{aligned} \tag{5.24}$$

and then we simplify, use the relation $g_1 = -2g_{2,s}$, and define the momentum to be $\Pi_s(x) = \partial_t\varphi_s(x)/v$ to get

$$\begin{aligned} H_s &= \frac{v}{2}\left(1 + \frac{g_{4,s} - g_{2,s}}{\pi}\right)\Pi_s^2 + \frac{v}{2}\left(1 + \frac{g_{4,s} + g_{2,s}}{\pi}\right)(\partial_x\varphi_s)^2 \\ &+ \frac{vg_1}{2\pi^2}\cos\left(\sqrt{8\pi}\varphi_s\right) \end{aligned} \tag{5.25}$$

At the end of this comparison we end up with the following conversion between Senechal's model, equation 7.19, and Nakamura or Giamarchi's model reproduced above in equation 5.2, through the following equivalences. The terms on the left are in Senechal's

notation while the terms on the right are Nakamura's.

$$\begin{aligned} v &= v_f \\ g_{4s} &= \frac{g_{4\parallel} - g_{4\perp}}{2v_f} \\ g_{2s} &= \frac{g_{1\parallel} - g_{2\parallel} + g_{2\perp}}{2v_f} \\ g_1 &= \frac{g_{1\perp}}{v_f} \\ g_{4c} &= \frac{g_{4\parallel} + g_{4\perp}}{2v_f} \\ g_{2c} &= \frac{g_{1\parallel} - g_{2\parallel} - g_{2\perp}}{2v_f} \\ g_3 &= \frac{g_{3\perp}}{v_f} \\ \varphi_s &= \frac{\phi_\sigma}{\sqrt{\pi}} \\ \varphi_c &= \frac{\phi_\rho}{\sqrt{\pi}} \end{aligned} \tag{5.26}$$

In [80], the spin-sector of the model is

$$\begin{aligned} H_s &= \int dx \frac{2\pi v_s}{3} [\vec{J_L}(x) \cdot \vec{J_L}(x) + \vec{J_R}(x) \cdot \vec{J_R}(x)] \\ &+ \lambda \int dx \vec{J_L}(x) \cdot \vec{J_R}(x). \end{aligned} \tag{5.27}$$

By direct comparison with [77] equations 7.18 to 7.20, we can determine the translation from [80] coefficients to [77], and then to the coefficients used in [75] and finally, in terms of the coefficients in the EHM, U and V.

First, let's translate from [80] to [77]. Below, the left side is [80] notation while the right side is [77].

$$\begin{aligned} v_s &= v\left(1+\frac{g_{4s}}{\pi}\right) \\ \lambda &= 4vg_{2,s} \\ U &= \frac{vg_3}{2\pi^2} \\ v_c &= v_c \\ K_c &= K_c \\ \phi_c &= \varphi_c \end{aligned} \tag{5.28}$$

Now we substitute the translations from [77] to [75], contained in equations 5.26, to get the translation from [80] to [75]:

$$\begin{aligned} v_s &= v_f + \frac{g_{4\parallel} - g_{4\perp}}{2\pi} \\ \lambda &= 2v_f g_{1\perp} \\ &= 2v_f(g_{1,\parallel} - g_{2,\parallel} + g_{2,\perp}) \\ U &= \frac{g_{3\perp}}{2\pi^2} \\ v_c &= v_\rho \\ K_c &= K_\rho \\ \phi_c &= \frac{\phi_\rho}{\sqrt{\pi}} \end{aligned} \tag{5.29}$$

I'm using Senechal's definitions for the currents. Note that the relationship for λ implies that we have a redundant coefficient in our g-ology, which originates in the SU(2) symmetry of the spin sector. Now, I'll write out these coefficients in terms of the g-ology

notation of [75]:

$$\begin{aligned} v_s &= v_f + \frac{g_{4\parallel} - g_{4\perp}}{2\pi} \\ \lambda &= 2v_f g_{1\perp} \\ &= 2v_f(g_{1,\parallel} - g_{2,\parallel} + g_{2,\perp}) \\ U &= \frac{g_{3\perp}}{2\pi^2} \\ v_c &= \sqrt{\left(v_f + \frac{g_{4\parallel} - g_{4\perp}}{2\pi}\right)^2 - \left(\frac{g_{1\parallel} - g_{2\parallel} + g_{2\perp}}{2\pi}\right)^2} \\ K_c &= \sqrt{\frac{2\pi v_f + g_{4\parallel} - g_{4\perp} + g_{1\parallel} - g_{2\parallel} + g_{2\perp}}{2\pi v_f + g_{4\parallel} - g_{4\perp} - g_{1\parallel} + g_{2\parallel} - g_{2\perp}}} \end{aligned} \tag{5.30}$$

where the corrected coefficients useful to our study were defined above in equation 5.7. This should now be sufficient to use [80]'s flows and our new initial conditions to begin running RG flows and see the BOW phase; if I trust the disorder part and the RG calculation, I can get straight to our full flows.

Completing the substitutions, including the corrected g-ology, we have

$$\begin{aligned} v_s &= v_f - \frac{U}{2\pi} \\ \lambda &= 2v_f g_{1\perp} \\ U_{FK} &= \frac{g_{3\perp}}{2\pi^2} \\ v_c &= \sqrt{(v_f - \frac{U}{2\pi})^2 - \left(\frac{2g_{1\perp}}{\pi}\right)^2} \\ K_c &= \sqrt{\frac{2\pi v_f - U + 4g_{1\perp}}{2\pi v_f - U - 4g_{1\perp}}}. \end{aligned} \tag{5.31}$$

One important point about equations 5.32 above is that v_s IS NOT the same as the usual spin field velocity that appears in bosonization, but instead it is just a coefficient

on the squared spin-current term in the Hamiltonian. As a result of this formulation, there is no need for K_s, a luttinger constant in the spin sector.

By comparing these coefficients with those presented in chapter 15 of [**?**], I modify them as follows:

$$\begin{aligned} v_s &= v_f - \frac{U}{2\pi} \\ \lambda &= 2g_{1\perp} \\ U_{FK} &= \frac{g_{3\perp}}{2\pi^2} \\ v_c &= \sqrt{(v_f - \frac{U}{2\pi})^2 - \left(\frac{2g_{1\perp}}{\pi}\right)^2} \\ K_c &= \sqrt{\frac{2\pi v_f - U + 4g_{1\perp}}{2\pi v_f - U - 4g_{1\perp}}}. \end{aligned} \tag{5.32}$$

5.4 Consistent notation: Disordered non-abelian model

In this section we derive the non-abelian form of the disorder backscattering in [80].

For this we need to know how the fundamental representation of SU(2) Lie algebra, $g(x)$, relates to the cosine of the spin field (although from [80] it is simply $tr(g)$)

5.5 Exercise: Incorporate high-energy modes into corrected g-ology

Following [79], I derive the corrected g-ology coefficients that split the single phase transition at U = 2V into two transitions, revealing a third phase between the two transitions. Also based on [81]. The value of this exercise is to gain general familiarity and

practice using Feynman diagrams at one loop and an overview from [81] of Fermi-liquid theory.

5.6 Exercise: Derive Sine-Gordon flow using OPE

This section will be based mostly on [77].

The main advantage of the technique colloquially called "operator product expansions" is that it uses results from conformal field theory to get to second order (1-loop) RG flow equations very quickly, bypassing the need for Feynman diagrams. I start by repeating equations A.1 to A.3 of [77] which is the bare minimum starting point needed to derive for myself the flow equations for the Sine-Gordon model.

Equation A.1 tells us a prescription for writing a perturbed action with the notation of "operators" (generally, functions of fields, derivatives of fields, or products of these):

$$\mathcal{S}(\varphi) = \mathcal{S}_0(\varphi) + \sum_i g_i \int dx d\tau \mathcal{O}_i(x,\tau) \tag{5.33}$$

Then, conformal feild theory says that products of operators can be rewritten as a series of operators multiplied by universal coefficients and an inverse power of distance between the points of application of the two operators:

$$\mathcal{O}_i(x)\mathcal{O}_j(x') = \sum_k C_{ij}^k \mathcal{O}_k(x') \frac{1}{|x-x'|^{\Delta_i+\Delta_j-\Delta_k}}. \tag{5.34}$$

The constants in the sum specify the quadratic terms in the RG flow:

$$\beta(g_k) = \frac{dg_k}{d\ell} = (2-\Delta_k)g_k - \sum_i C_{ijk} g_j g_k. \tag{5.35}$$

This set of equations above provides us with a prescription to get directly from a perturbed Hamiltonian to an RG flow, and all we need for this is to get the coefficients from the operator product expansion.

Now I will complete this exercise for an interacting, bosonized hamiltonian (which results in a sine-Gordon model). I'll start with the generic bosonized lagrangian, equation 6.6 from [77], with the index removed, including a general interaction, equation 5.66. [77].

$$\mathcal{L} = \int dx \left[\frac{1}{2K} \left(\frac{1}{v} \left(\partial_t \varphi \right)^2 - v \left(\partial_x \varphi \right)^2 \right) - \frac{v_f g}{2\pi^2} \cos\left(\sqrt{8\pi} \varphi \right) \right] \tag{5.36}$$

Note the distinction between v_f and v – v has been altered from v_f due to the interactions incorporated into the bosonic theory.

Now I'll manipulate this into a sum of coefficients times perturbing operators. In order to force K and v into the role of operator coefficients (parameters that participate in the RG flow), I'll peel the factor of 1/K off the "unperturbed" lagrangian and turn it into a perturbation:

$$\begin{aligned} \mathcal{L}_0 &= \frac{1}{2} \int dx \left[\frac{1}{v} \left(\partial_t \varphi \right)^2 - v \left(\partial_x \varphi \right)^2 \right] \\ \mathcal{L}' &= \int dx \left[\frac{1-K}{2K} \left(\frac{1}{v} \left(\partial_t \varphi \right)^2 - v \left(\partial_x \varphi \right)^2 \right) - \frac{v_f g}{2\pi^2} \cos\left(\sqrt{8\pi} \varphi \right) \right] \end{aligned} \tag{5.37}$$

This model has two operators. The free field portion of $\mathcal{H}$ can be defined as a single operator in the complex plane (see [77] appendix A)

$$\mathcal{O}_1 = \partial_z \phi \partial_{\bar{z}} \phi \tag{5.38}$$

with a corresponding coefficient 2k. The cosine term gives our second operator,

$$\mathcal{O}_2 = \cos(\phi) \tag{5.39}$$

.

with corresponding coefficient u. Next we need the scaling exponents for the two operators, Δ_i, and the universal OPE coefficients, C_{nmk}.

Starting with the free-field term, it has scaling dimension 2, which is by design (it sets the definition of relevant and irrelevant).

$$\Delta_1 = 2 \tag{5.40}$$

Next, the scaling dimension of the cosine is the same as that of a vertex operator (exponential operator), which I evaluated using equations 5.32 of [77] to give

$$\Delta_2 = \frac{1}{4\pi} \tag{5.41}$$

5.7 Exercise: Use the OPE to derive Sine-Gordon RG

Here I use [82][83] for the 2D XY model and derivations in [77], section 6.4 and Appendix A, and [84], chapter 4 to develop an understanding of the sine-Gordon renormalization group flow equations. With this understanding, I can derive the correct flow equations for our problem of interest.

First we start with the bosonic form of the spin-sector Hamiltonian density, including a term for the $g_{1,\perp}$ interaction (since $g_{1,\parallel}$ is incorporated into forward scattering, we let $g_1 \equiv g_{1,\perp}$) that becomes a sine-Gordon model ([77] eq. 6.25)

$$\mathcal{H}_{spin} = \frac{v_s}{2}[K_s\Pi_s(x)^2 + \frac{1}{K_s}\partial_x\varphi_s(x)^2] + \frac{v_s g_1}{2\pi^2}\cos(\sqrt{8\pi}\varphi_s(x)) \tag{5.42}$$

.

The fields can then be rescaled to remove the spin stiffness constant K_s from the kinetic portion (see [**?**] equation 6.7).

$$\mathcal{H}_{spin} = \frac{v_s}{2}[\Pi_s'(x)^2 + \partial_x\varphi_s'(x)^2] + \frac{v_s g_1}{2\pi^2}\cos(\sqrt{8\pi K_s}\varphi_s') \tag{5.43}$$

For the rest of this section, set v_s equal to 1, since it won't affect this particular RG analysis. When including additional terms to the model, v_s is no longer an arbitrary constant.

At this point we want to use the path integral formalism to treat the nonlinear term perturbatively. Start by transforming the Hamiltonian density to a Lagrangian density; we get

$$\mathcal{L}_{SG} = \frac{1}{2}((\partial_t\phi)^2 - (\partial_x\phi)^2) - \frac{g_1}{2\pi^2}\cos(\sqrt{8\pi K_s}\phi) \tag{5.44}$$

Redefine the coefficients and fields‘ so that $k = 1/8\pi K_s$ and $u = g_1/2\pi^2$ and the model takes the form

$$\mathcal{L}_{SG} = \frac{k}{2}((\partial_t\phi)^2 - (\partial_x\phi)^2) - u\cos(\phi) \tag{5.45}$$

.

With our Lagrangian density we write down a path integral over the field fluctuations

$$\mathcal{U}(x_f, t_f; x_i, t_i) = \int \mathcal{D}[\phi(x,t)]e^{\frac{i}{\hbar}\int_0^L\int_{t_0}^{t_f} dxdt\mathcal{L}[\phi(x,t)]} \tag{5.46}$$

.

After substituting $\tau = -it$ and $\mathcal{L}$ explicitly in the action integral exponent, the path integral takes the form of a partition function for a classical field in two Euclidean dimensions,

$$\mathcal{U}(x_f, \tau_f; x_i, \tau_i) = \int \mathcal{D}[\phi(x,\tau)] e^{\frac{-1}{\hbar}\int_0^L \int_{\tau_0}^{\tau_f} dx d\tau \left(\frac{k}{2}\left[(\partial_\tau \phi)^2 + (\partial_x \phi)^2\right] + u\cos(\phi)\right)} \tag{5.47}$$

.

Our goal is to perform a real-space renormalization analysis on the above path integral to get an effective model. Or more precisely, we want to derive beta functions for the above model that can then be used to derive the effective low-energy, long-wavelength physics of the model. Following the methods of both T+F and F+K, we do this using the Operator Product Expansion method, although the results would be the same as with a momentum-shell renormalization (that is, using Feynman diagrams, included in the Appendix as an exercise and comparison).

Chapter 6

Renormalization Group Flows

First, I present a table of the sanity check results from the flows. The descriptions of the expected flows are included in the first chapter of this section 3.

Here we present some data tables to summarize the observations.

	$U < 2V$	$U = 2V$	$U > 2V$
$\Delta < max(U, 2V)$			
$\Delta = max(U, 2V)$			
$\Delta > max(U, 2V)$			

U	**V**	Δ	**Phase**	**Indicators**	**Reference**	**Verified?**
0	0	0	Metal			
U >	2V	0	SDW - Ref?			
U <	2V	0	CDW - Ref?			
U	0	$\Delta <$	Mott FK			
U		$\Delta >$	Anderson FK			
U		Critical	Mott/And FK			
U =	2V	0	BOW - TF			

6.1 Practice RG flows for BOW using Abelian model

Here I practice the basic approach for weak coupling, as follows from flow equations 3.1 - 3.3 derived from equations 2.19, following [79].

$$\begin{aligned}
\mathcal{H}_0 &= \frac{1}{2\pi}\sum_{p=+,-}\left[\upsilon_\rho\left(\partial_x\theta_p\right)^2+\upsilon_\sigma\left(\partial_x\phi_p\right)^2\right] \\
&+\frac{g_\rho}{2\pi^2}\left(\partial_x\theta_+\right)\left(\partial_x\theta_-\right)-\frac{g_\sigma}{2\pi^2}\left(\partial_x\phi_+\right)\left(\partial_x\phi_-\right) \\
&-\frac{g_c}{2\pi^2a^2}cos(2\theta)+\frac{g_s}{2\pi^2a^2}cos(2\phi) \\
&-\frac{g_{cs}}{2\pi^2a^2}cos(2\theta)cos(2\phi)-\frac{g_{\rho s}}{2\pi^2}\left(\partial_x\theta_+\right)\left(\partial_x\theta_-\right)cos(2\phi) \\
&+\frac{g_{c\sigma}}{2\pi^2}\left(\partial_x\phi_+\right)\left(\partial_x\phi_-\right)cos(2\theta) \\
&+\frac{g_{\rho\sigma}a^2}{2\pi^2}\left(\partial_x\theta_+\right)\left(\partial_x\theta_-\right)\left(\partial_x\phi_+\right)\left(\partial_x\phi_-\right), \qquad (6.1)
\end{aligned}$$

For U,V << t, we can neglect all operators with scaling dimension 4 and higher. This includes terms with a coefficient that has a single subscript (υ_σ or g_s for example). Meanwhile, all terms with two subscripts couple spin and charge. Reference [79] uses an operator product expansion to derive renormalization group equations, including all terms in 6.1.

Here I reproduce one of those operator product expansions (to be completed if necessary)

By neglecting the dimension 4 operators, the following flow equations result:

$$\partial_l G_\rho(l) = 2G_c(l)^2 \qquad (6.2)$$

$$\partial_l G_c(l) = 2G_\rho(l)G_c(l) \qquad (6.3)$$

$$\partial_l G_s(l) = -2G_s(l)^2, \qquad (6.4)$$

with initial conditions determined by

$$
\begin{aligned}
\upsilon_\rho &= 2ta + (g_{4\parallel} + g_{4\perp} - g_{1\parallel}) = 6V + U \\
\upsilon_\sigma &= 2ta + (g_{4\parallel} - g_{4\perp} - g_{1\parallel}) = 2V - U \\
g_\rho &= g_{2\perp} + g_{2\parallel} - g_{1\parallel} = 6V + U \\
g_\sigma &= g_{2\perp} - g_{2\parallel} + g_{1\parallel} = U - 2V \\
g_c &= g_{3\perp} = U - 2V + \delta \\
g_s &= g_{1\perp} = U - 2V - \delta
\end{aligned} \tag{6.5}
$$

In these equations, G_i is just a dimensionless coupling, $g_i/4\pi t$. The flow initial conditions, $G_i(0)$, are simply the coefficients in 6.1, which in turn depend on U and V. For completeness I list these dependencies in equation 6.5. To identify a particular phase, one runs an iterative differential equation solver and observes (usually by automation (!)) which coefficients diverge. To extract the correct thermodynamic phase from a flow, [79] considers the effect the divergent cos() term will have on the fields, θ or ϕ, locking them to some multiples of $\pi/2$. These locked fields force the order parameters to be 0 except in the phase of interest. I include the order parameters in equation 6.6 (in Ref. [79] these correspond to equation 2.18).

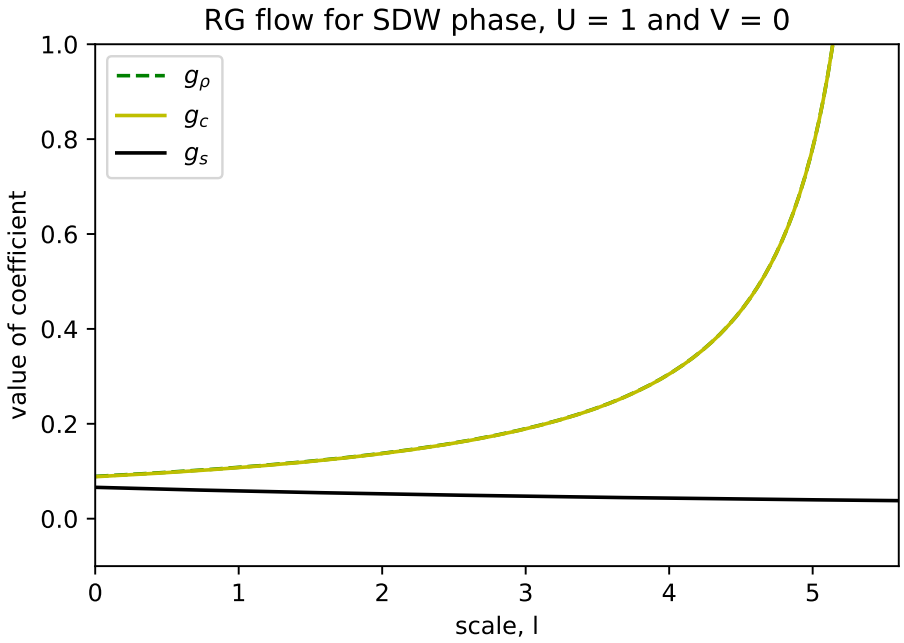

Figure 6.1: A SDW flow

$$\begin{aligned}
\mathcal{O}_{SDW}(x) &= cos(\theta(x))sin(\phi(x)) \\
\mathcal{O}_{CDW}(x) &= sin(\theta(x))cos(\phi(x)) \\
\mathcal{O}_{BCDW}(x) &= cos(\theta(x))cos(\phi(x)) \\
\mathcal{O}_{BSDW}(x) &= sin(\theta(x))sin(\phi(x))
\end{aligned} \tag{6.6}$$

In the SDW phase, a typical flow generated from these equations looks like figure 6.1. The SDW phase is gapped to charge excitations, so we expect g_c to diverge, but gapless to spin excitations, so g_s converges to 0. Note that g_ρ and g_c are equal and both diverge. In

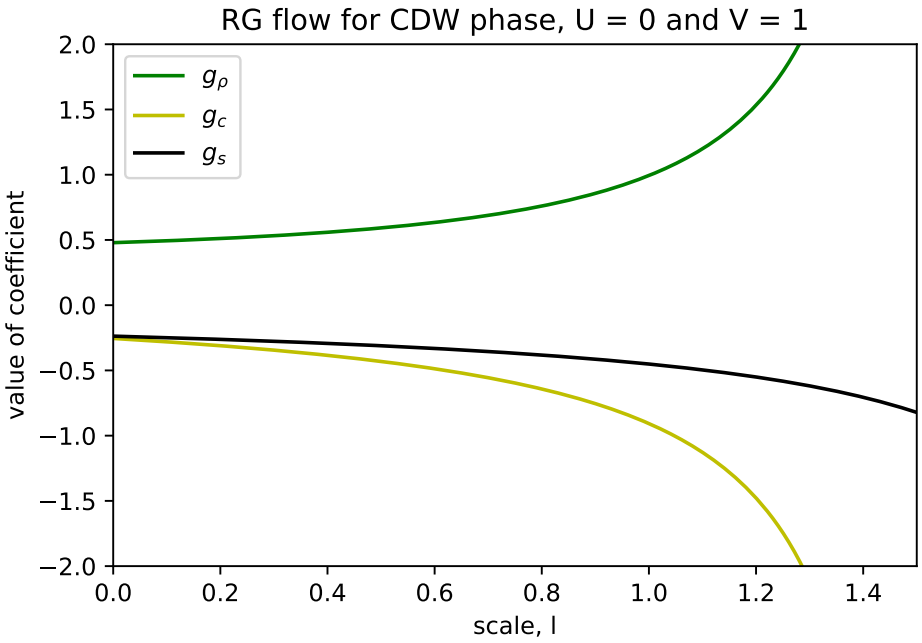

Figure 6.2: A CDW flow

the CDW phase, a typical flow looks like figure 6.2. This flow is characterized by negative g_s which diverges strongly and negative g_c which also diverges strongly, while $|g_s| = g_c$.

I used an automated loop to compute a grid of 100 by 100 points in the (U,V) plane and identify the RG flows as CDW or SDW, labeled by a color map. Since there are no corrections in the g-ology for this flow, there is only a single phase transition and no BOW phase. This is shown in figure 6.3.

After adding the corrections developed in Ref. [79] to the g-ology, the result is figure 6.5 reproducing the weak-coupling results in [79]. A typical flow for the BOW phase is shown in figure 6.4. The BOW phase is characterized by positive umklapp and negative backscattering coefficients, $4\pi t G_c(0) = g_c = g_{3\perp}$ and $4\pi t G_s(0) = g_s = g_{1\perp}$ which both

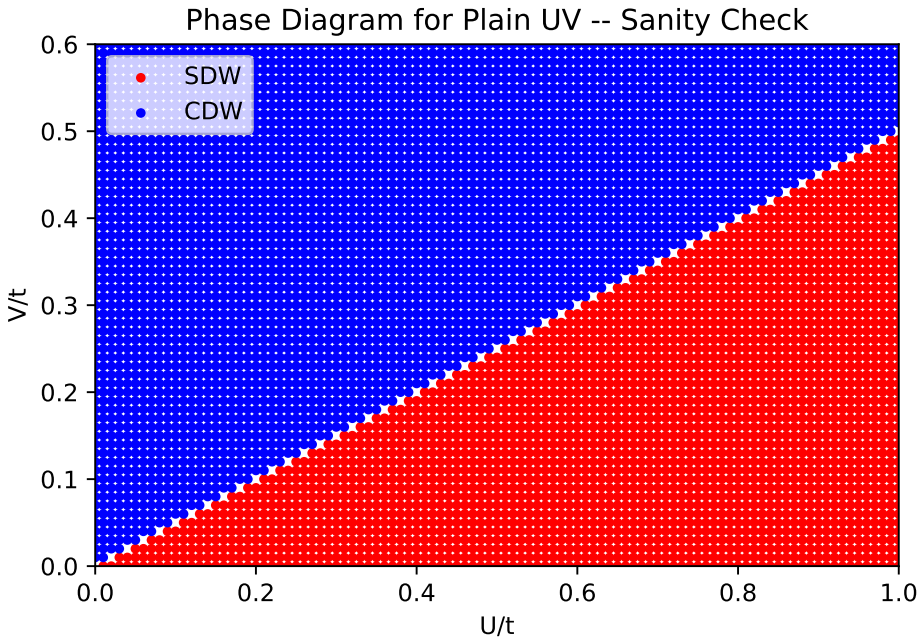

Figure 6.3: Grid of flow results without corrections for BOW

diverge. However, in the BOW phase, the negative backscattering coefficient g_s will not grow appreciably until a scale of about $l = 50$. This implies we have to be careful, as this coefficient may appear irrelevant while other coefficients diverge, even though it is in fact relevant.

This is illustrated in figure 6.4, where at the values of scale shown, g_s appears to remain fixed at a small negative value, even though it will eventually diverge. This provides a clear lesson in the need to interpret RG flows carefully.

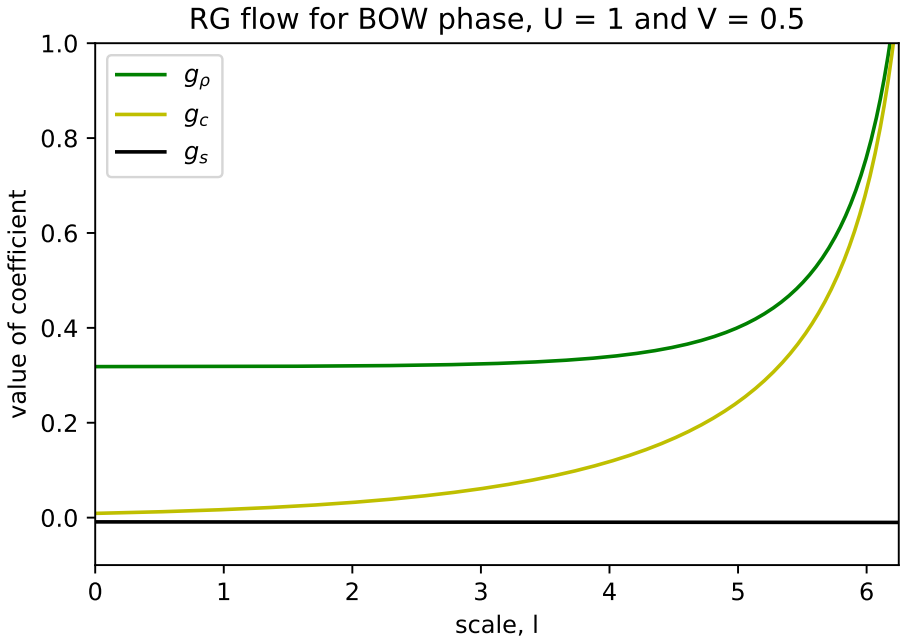

Figure 6.4: A BOW flow

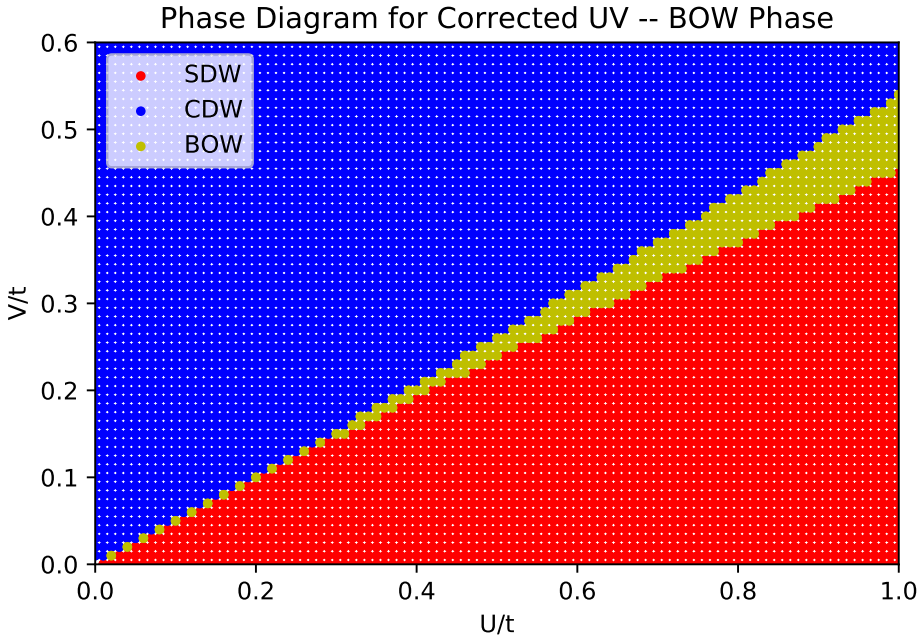

Figure 6.5: Flow results for BOW with corrections

6.1.1 Exercise: Negative U and V – Standardized notation

We know from prior works [75] that the negative U and V cases lead to various delocalized, superconducting phases. Studying these will help support investigating the phases we observe when disorder is added.

6.2 RG for Non-Abelian model with disorder

In the second section, I present the results of RG flows for the non-Abelian, disordered model from [80], with coefficients determined in a previous Chapter 5 equation 5.32. Below I repeat the RG flows from [80] for ease of reference.

$$\frac{d\underline{D_\xi}}{dl} = (2 - K_\rho - 3\underline{\lambda})\underline{D_\xi} \tag{6.7}$$

$$\frac{d\underline{D_\eta}}{dl} = \underline{D_\eta} + 4\pi^2 g(u)\underline{D_\xi}^2 \tag{6.8}$$

$$\frac{d\underline{D_A}}{dl} = \underline{D_A} + 4\pi^2 g(u)\underline{D_\xi}^2 \tag{6.9}$$

$$\frac{d\underline{U}}{dl} = (2 - 2K_c)\underline{U} - \frac{4}{\pi^2}\underline{D_\eta}K_c^2\underline{U} \tag{6.10}$$

$$\frac{d\underline{\lambda}}{dl} = -\frac{\underline{\lambda}^2}{2} - \underline{D_\xi} \tag{6.11}$$

$$\frac{dK_c}{dl} = -2\pi K_c^2\underline{U}^2 - \frac{K_c^2\underline{D_\xi}}{2u} \tag{6.12}$$

$$\frac{dv_c}{dl} = -\frac{\pi K_c\underline{D_\xi}v_c}{2u} \tag{6.13}$$

$$\frac{du}{dl} = -u\underline{D_\xi}, \tag{6.14}$$

where $g(x) = [\int_{-\infty}^{\infty} \frac{dy}{\sqrt{1+x^2y^2}(1+y^2)^{Kc/2}}]^2$, $\underline{D} = D/v_c^2$, $\underline{U} = U/v_c$, $\underline{\lambda} = \lambda/v_s$, $u = v_s/v_c$.

6.2.1 Check flows when $\Delta = 0$

In this section I'll study flows for the above equations when the initial disorder amplitude, $D_\xi = D_\eta = \Delta = 0$, and the other initial conditions are set previously in equations 5.32 for appropriate values of U and V.

SDW, U = 1, V = 0

In the SDW phase, I expect the SDW order parameter to be maximized:

$$\mathcal{O}_{SDW} = (-1)^j (n_{\uparrow,j} - n_{\downarrow,j}) \tag{6.15}$$

This notation needs to be translated into operators appropriate to our model so that we can evaluate which terms become relevant in the renormaliztion group flows.

Chapter 7

Outlook

The combination of disorder and interactions provides a challenging forefront for condensed matter theory. Extensions to this project include "straightforward" extensions to additional models and parameter regimes; focusing in on particular phase transition lines; or changing the distribution of the disorder. A less straightforward direction is to formulate the problem as a functional Renormalization Group calculation.

A more challenging task is to supplement these analytical approaches with DMRG, which can tackle parameter regimes not approachable analytically, while also providing a second viewpoint to confirm or reject the observations performed analytically. There are a large number of DMRG methods adapted to disorder, and I have some thoughts on what to do for this problem.

Lastly, applying the information theory perspective to the disorder problem would provide an exciting opportunity.

Bibliography

[1] J. Spalding, S.-W. Tsai, and D. K. Campbell, "Critical entanglement for the half-filled extended hubbard model", Phys. Rev. B **99**, 195445 (2019), DOI: 10.1103/PhysRevB.99.195445, URL https://link.aps.org/doi/10.1103/PhysRevB.99.195445.

[2] F. H. Essler, H. Frahm, F. Göhmann, A. Klümper, and V. E. Korepin, *The one-dimensional Hubbard model*, (Cambridge University Press, 2005).

[3] S. Ejima and S. Nishimoto, "Phase diagram of the one-dimensional half-filled extended hubbard model", Phys. Rev. Lett. **99**(21), 216403 (2007).

[4] T. Ishiguro, K. Yamaji, and G. Saito, *Organic superconductors*, volume 88, (Springer Science & Business Media, 2012).

[5] D. Baeriswyl, D. Campbell, G. Clark, G. Harbeke, P. Kahol, H. Kiess, S. Mazumdar, M. Mehring, and W. Rehwald, *Conjugated conducting polymers*, volume 102, (Springer Science & Business Media, 2012).

[6] H. Ishii, H. Kataura, H. Shiozawa, H. Yoshioka, H. Otsubo, Y. Takayama, T. Miyahara, S. Suzuki, Y. Achiba, M. Nakatake, et al., "Direct observation of tomonaga–luttinger-liquid state in carbon nanotubes at low temperatures", Nature **426**(6966), 540 (2003).

[7] D. Jaksch and P. Zoller, "The cold atom hubbard toolbox", Annals of Physics **315**(1), 52 – 79 (2005), DOI: https://doi.org/10.1016/j.aop.2004.09.010, special Issue.

[8] S. Baier, M. J. Mark, D. Petter, K. Aikawa, L. Chomaz, Z. Cai, M. Baranov, P. Zoller, and F. Ferlaino, "Extended bose-hubbard models with ultracold magnetic atoms", Science **352**(6282), 201–205 (2016), DOI: 10.1126/science.aac9812.

[9] S. Murmann, A. Bergschneider, V. M. Klinkhamer, G. Zürn, T. Lompe, and S. Jochim, "Two fermions in a double well: Exploring a fundamental building block of the hubbard model", Phys. Rev. Lett. **114**(8), 080402 (2015).

[10] C. Gross and I. Bloch, "Quantum simulations with ultracold atoms in optical lattices", Science **357**(6355), 995–1001 (2017), DOI: 10.1126/science.aal3837, URL http://science.sciencemag.org/content/357/6355/995.

[11] T. Hensgens, T. Fujita, L. Janssen, X. Li, C. Van Diepen, C. Reichl, W. Wegscheider, S. D. Sarma, and L. M. Vandersypen, "Quantum simulation of a fermi–hubbard model using a semiconductor quantum dot array", Nature **548**(7665), 70 (2017).

[12] R. Islam, R. Ma, P. M. Preiss, M. E. Tai, A. Lukin, M. Rispoli, and M. Greiner, "Measuring entanglement entropy in a quantum many-body system", Nature **528**(7580), 77 (2015).

[13] S. R. White, "Density matrix formulation for quantum renormalization groups", Physical review letters **69**(19), 2863 (1992).

[14] S. R. White, "Density-matrix algorithms for quantum renormalization groups", Physical Review B **48**(14), 10345 (1993).

[15] U. Schollwöck, "The density-matrix renormalization group in the age of matrix product states", Annals of Physics **326**(1), 96 – 192 (2011), DOI: https://doi.org/10.1016/j.aop.2010.09.012, URL http://www.sciencedirect.com/science/article/pii/S0003491610001752, january 2011 Special Issue.

[16] A. Griesmaier, J. Werner, S. Hensler, J. Stuhler, and T. Pfau, "Bose-Einstein Condensation of Chromium", Phys. Rev. Lett. **94**(16), 160401 (2005), DOI: 10.1103/PhysRevLett.94.160401.

[17] K. Aikawa, A. Frisch, M. Mark, S. Baier, A. Rietzler, R. Grimm, and F. Ferlaino, "Bose-Einstein Condensation of Erbium", Phys. Rev. Lett. **108**, 210401 (2012).

[18] K. Aikawa, A. Frisch, M. Mark, S. Baier, R. Grimm, and F. Ferlaino, "Reaching Fermi Degeneracy via Universal Dipolar Scattering", Phys. Rev. Lett. **112**(1), 010404 (2014), DOI: 10.1103/PhysRevLett.112.010404.

[19] M. Lu, N. Q. Burdick, S. H. Youn, and B. L. Lev, "Strongly Dipolar Bose-Einstein Condensate of Dysprosium", Phys. Rev. Lett. **107**(19), 190401 (2011), DOI: 10.1103/PhysRevLett.107.190401.

[20] M. Lu, N. Q. Burdick, and B. L. Lev, "Quantum Degenerate Dipolar Fermi Gas", Phys. Rev. Lett. **108**(21), 215301 (2012), DOI: 10.1103/PhysRevLett.108.215301.

[21] Y. Tang, N. Q. Burdick, K. Baumann, and B. L. Lev, "Bose-Einstein condensation of 162Dy and 160Dy", New. J. Phys. **17**, 045006 (2015).

[22] K.-K. Ni, S. Ospelkaus, M. H. G. de Miranda, A. Pe'er, B. Neyenhuis, J. J. Zirbel, S. Kotochigova, P. S. Julienne, D. S. Jin, and J. Ye, "A High Phase-Space-Density Gas of Polar Molecules", Science **322**, 231– (2008), DOI: 10.1126/science.1163861.

[23] A. Chotia, B. Neyenhuis, S. A. Moses, B. Yan, J. P. Covey, M. Foss-Feig, A. M. Rey, D. S. Jin, and J. Ye, "Long-Lived Dipolar Molecules and Feshbach Molecules in a 3D Optical Lattice", Phys. Rev. Lett. **108**(8), 080405 (2012), DOI: 10.1103/PhysRevLett.108.080405.

[24] J. F. Barry, D. J. McCarron, E. B. Norrgard, M. H. Steinecker, and D. DeMille, "Magneto-optical trapping of a diatomic molecule", Nature **512**(7514), 286–289 (2014), DOI: 10.1038/nature13634, URL http://www.nature.com/articles/nature13634.

[25] D. J. McCarron, M. H. Steinecker, Y. Zhu, and D. DeMille, "Magnetically-Trapped Molecules Efficiently Loaded from a Molecular MOT", Phys. Rev. Lett. **121**, 013202 (2018), DOI: https://arxiv.org/abs/1712.01462, URL https://arxiv.org/abs/1712.01462.

[26] M. T. Hummon, M. Yeo, B. K. Stuhl, A. L. Collopy, Y. Xia, and J. Ye, "2D Magneto-Optical Trapping of Diatomic Molecules", Phys. Rev. Lett. **110**(14), 143001 (2013), DOI: 10.1103/PhysRevLett.110.143001, URL https://link.aps.org/doi/10.1103/PhysRevLett.110.143001.

[27] L. Anderegg, B. L. Augenbraun, Y. Bao, S. Burchesky, L. W. Cheuk, W. Ketterle, and J. M. Doyle, "Laser Cooling of Optically Trapped Molecules", Nature Phys. **14**, 890 (2018), URL http://arxiv.org/abs/1803.04571.

[28] B. Hemmerling, E. Chae, A. Ravi, L. Anderegg, G. K. Drayna, N. R. Hutzler, A. L. Collopy, J. Ye, W. Ketterle, and J. M. Doyle, "Laser slowing of CaF molecules to near the capture velocity of a molecular MOT", J. Phys. B: At., Mol. Opt. Phys. **49**(17), 174001 (2016), DOI: 10.1088/0953-4075/49/17/174001, URL http://stacks.iop.org/0953-4075/49/i=17/a=174001?key=crossref.447f9ecba3b1cb0b91c5968a1d3efcf9.

[29] M. Nakamura, "Tricritical behavior in the extended hubbard chains", Phys. Rev. B **61**, 16377–16392 (2000), DOI: 10.1103/PhysRevB.61.16377, URL http://link.aps.org/doi/10.1103/PhysRevB.61.16377.

[30] M. Tsuchiizu and A. Furusaki, "Phase diagram of the one-dimensional extended hubbard model at half filling", Phys. Rev. Lett. **88**, 056402 (2002), DOI: 10.1103/PhysRevLett.88.056402, URL https://link.aps.org/doi/10.1103/PhysRevLett.88.056402.

[31] K.-M. Tam, S.-W. Tsai, and D. K. Campbell, "Functional renormalization group analysis of the half-filled one-dimensional extended hubbard model", Phys. Rev. Lett. **96**(3), 036408 (2006).

[32] S. Ejima, F. H. L. Essler, F. Lange, and H. Fehske, "Ising tricriticality in the extended hubbard model with bond dimerization", Phys. Rev. B **93**, 235118 (2016), DOI: 10.1103/PhysRevB.93.235118, URL https://link.aps.org/doi/10.1103/PhysRevB.93.235118.

[33] A. W. Sandvik, L. Balents, and D. K. Campbell, "Ground state phases of the half-filled one-dimensional extended hubbard model", Phys. Rev. Lett. **92**, 236401 (2004), DOI: 10.1103/PhysRevLett.92.236401, URL http://link.aps.org/doi/10.1103/PhysRevLett.92.236401.

[34] Y. Zhang, "Dimerization in a half-filled one-dimensional extended hubbard model", Phys. Rev. Lett. **92**(24), 246404 (2004).

[35] S. Glocke, A. Klümper, and J. Sirker, "Half-filled one-dimensional extended hubbard model: Phase diagram and thermodynamics", Phys. Rev. B **76**(15), 155121 (2007).

[36] S. Ejima and S. Nishimoto, "Ground-state properties of the one-dimensional extended hubbard model at half filling", Journal of Physics and Chemistry of Solids **69**(12), 3293–3296 (2008).

[37] M. Ménard and C. Bourbonnais, "Renormalization group analysis of the one-dimensional extended hubbard model", Phys. Rev. B **83**, 075111 (2011), DOI: 10.1103/PhysRevB.83.075111, URL https://link.aps.org/doi/10.1103/PhysRevB.83.075111.

[38] P. Sengupta, A. W. Sandvik, and D. K. Campbell, "Bond-order-wave phase and quantum phase transitions in the one-dimensional extended hubbard model", Physical Review B **65**(15), 155113 (2002).

[39] E. Jeckelmann, "Ground-state phase diagram of a half-filled one-dimensional extended hubbard model", Phys. Rev. Lett. **89**, 236401 (2002), DOI: 10.1103/PhysRevLett.89.236401, URL https://link.aps.org/doi/10.1103/PhysRevLett.89.236401.

[40] M. Dalmonte, J. Carrasquilla, L. Taddia, E. Ercolessi, and M. Rigol, "Gap scaling at berezinskii-kosterlitz-thouless quantum critical points in one-dimensional hubbard and heisenberg models", Physical Review B **91**(16), 165136 (2015).

[41] B. Pirvu, G. Vidal, F. Verstraete, and L. Tagliacozzo, "Matrix product states for critical spin chains: Finite-size versus finite-entanglement scaling", Phys. Rev. B **86**, 075117 (2012), DOI: 10.1103/PhysRevB.86.075117, URL https://link.aps.org/doi/10.1103/PhysRevB.86.075117.

[42] M. Hafez-Torbati and G. S. Uhrig, "Singlet exciton condensation and bond-order-wave phase in the extended hubbard model", Phys. Rev. B **96**, 125129 (2017), DOI: 10.1103/PhysRevB.96.125129, URL https://link.aps.org/doi/10.1103/PhysRevB.96.125129.

[43] H. Krull, N. Drescher, and G. Uhrig, "Enhanced perturbative continuous unitary transformations", Phys. Rev. B **86**(12), 125113 (2012).

[44] S. Chen, L. Wang, S.-J. Gu, and Y. Wang, "Fidelity and quantum phase transition for the heisenberg chain with next-nearest-neighbor interaction", Physical Review E **76**(6), 061108 (2007).

[45] L. Amico, R. Fazio, A. Osterloh, and V. Vedral, "Entanglement in many-body systems", Rev. Mod. Phys. **80**(2), 517 (2008).

[46] C. Mund, Ö. Legeza, and R. Noack, "Quantum information analysis of the phase diagram of the half-filled extended hubbard model", Phys. Rev. B **79**(24), 245130 (2009).

[47] S. Nishimoto, "Tomonaga-luttinger-liquid criticality: Numerical entanglement entropy approach", Phys. Rev. B **84**, 195108 (2011), DOI: 10.1103/PhysRevB.84.195108, URL https://link.aps.org/doi/10.1103/PhysRevB.84.195108.

[48] A. M. Kaufman, M. E. Tai, A. Lukin, M. Rispoli, R. Schittko, P. M. Preiss, and M. Greiner, "Quantum thermalization through entanglement in an isolated many-body system", Science **353**(6301), 794–800 (2016).

[49] A. Bazavov, Y. Meurice, S.-W. Tsai, J. Unmuth-Yockey, L.-P. Yang, and J. Zhang, "Estimating the central charge from the rényi entanglement entropy", Phys. Rev. D **96**, 034514 (2017), DOI: 10.1103/PhysRevD.96.034514, URL https://link.aps.org/doi/10.1103/PhysRevD.96.034514.

[50] J. Unmuth-Yockey, J. Zhang, P. M. Preiss, L.-P. Yang, S.-W. Tsai, and Y. Meurice, "Probing the conformal calabrese-cardy scaling with cold atoms", Phys. Rev. A **96**, 023603 (2017), DOI: 10.1103/PhysRevA.96.023603, URL https://link.aps.org/doi/10.1103/PhysRevA.96.023603.

[51] S.-W. Tsai and J. Marston, "Density-matrix renormalization-group analysis of quantum critical points: Quantum spin chains", Phys. Rev. B **62**(9), 5546 (2000).

[52] S. Ejima and S. Nishimoto, "Phase diagram of the one-dimensional half-filled extended hubbard model", Phys. Rev. Lett. **99**, 216403 (2007), DOI: 10.1103/PhysRevLett.99.216403, URL http://link.aps.org/doi/10.1103/PhysRevLett.99.216403.

[53] H. Nishimori and G. Ortiz, *Elements of Phase Transitions and Critical Phenomena*, (Oxford University Press, 2011).

[54] S. Sachdev, *Quantum Phase Transitions, Second Edition*, (Cambridge University Press, 2011).

[55] J. Cardy, *Scaling and Renormalization in Statistical Physics*, (Cambridge University Press, 1996).

[56] C. Holzhey, F. Larsen, and F. Wilczek, "Geometric and renormalized entropy in conformal field theory", Nuclear Physics B **424**(3), 443–467 (1994).

[57] G. Vidal, J. I. Latorre, E. Rico, and A. Kitaev, "Entanglement in quantum critical phenomena", Physical review letters **90**(22), 227902 (2003).

[58] V. Korepin, "Universality of entropy scaling in one dimensional gapless models", Physical review letters **92**(9), 096402 (2004).

[59] P. Calabrese and J. Cardy, "Entanglement entropy and quantum field theory", Journal of Statistical Mechanics: Theory and Experiment **2004**(06), P06002 (2004), URL http://stacks.iop.org/1742-5468/2004/i=06/a=P06002.

[60] N. Laflorencie, E. S. Sørensen, M.-S. Chang, and I. Affleck, "Boundary effects in the critical scaling of entanglement entropy in 1d systems", Phys. Rev. Lett. **96**, 100603 (2006), DOI: 10.1103/PhysRevLett.96.100603, URL https://link.aps.org/doi/10.1103/PhysRevLett.96.100603.

[61] I. Affleck, N. Laflorencie, and E. S. Sorensen, "Entanglement entropy in quantum impurity systems and systems with boundaries", J. of Phys. A: Math. Theor. **42**, 504009 (2009).

[62] P. Calabrese, M. Campostrini, F. Essler, and B. Nienhuis, "Parity effects in the scaling of block entanglement in gapless spin chains", Phys. Rev. Lett. **104**, 095701 (2010), DOI: 10.1103/PhysRevLett.104.095701, URL https://link.aps.org/doi/10.1103/PhysRevLett.104.095701.

[63] S. R. White, I. Affleck, and D. J. Scalapino, "Friedel oscillations and charge density waves in chains and ladders", Phys. Rev. B **65**, 165122 (2002), DOI: 10.1103/PhysRevB.65.165122, URL https://link.aps.org/doi/10.1103/PhysRevB.65.165122.

[64] J. Cardy and P. Calabrese, "Unusual corrections to scaling in entanglement entropy", Journal of Statistical Mechanics: Theory and Experiment **2010**(04), P04023 (2010), URL http://stacks.iop.org/1742-5468/2010/i=04/a=P04023.

[65] A. B. Zamolodchikov, "Irreversibility of the flux of the renormalization group in a 2d field theory", JETP Lett. **43**, 731 (1986).

[66] D. K. Campbell, *Historical Overview of the* Φ^4 *Model*, (Springer).

[67] V. V. França and K. Capelle, "Universal and nonuniversal contributions to block-block entanglement in many-fermion systems", Phys. Rev. A **77**, 062324 (2008), DOI: 10.1103/PhysRevA.77.062324, URL https://link.aps.org/doi/10.1103/PhysRevA.77.062324.

[68] M. Vekić and S. R. White, "Smooth boundary conditions for quantum lattice systems", Phys. Rev. Lett. **71**, 4283–4286 (1993), DOI: 10.1103/PhysRevLett.71.4283, URL https://link.aps.org/doi/10.1103/PhysRevLett.71.4283.

[69] W. Zhang, S. Greschner, E. Fan, T. C. Scott, and Y. Zhang, "Ground-state properties of the one-dimensional unconstrained pseudo-anyon hubbard model", Phys. Rev. A **95**, 053614 (2017), DOI: 10.1103/PhysRevA.95.053614, URL https://link.aps.org/doi/10.1103/PhysRevA.95.053614.

[70] T. Durić, K. Biedroń, and J. Zakrzewski, "Fibonacci anyon excitations of one-dimensional dipolar lattice bosons", Phys. Rev. B **95**, 085102 (2017), DOI: 10.1103/PhysRevB.95.085102, URL https://link.aps.org/doi/10.1103/PhysRevB.95.085102.

[71] S. Miyakoshi, S. Nishimoto, and Y. Ohta, "Entanglement properties of the haldane phases: A finite system-size approach", Phys. Rev. B **94**, 235155 (2016), DOI: 10.1103/PhysRevB.94.235155, URL https://link.aps.org/doi/10.1103/PhysRevB.94.235155.

[72] S. Ejima, F. Lange, and H. Fehske, "Spectral and entanglement properties of the bosonic haldane insulator", Phys. Rev. Lett. **113**, 020401 (2014), DOI: 10.1103/PhysRevLett.113.020401, URL https://link.aps.org/doi/10.1103/PhysRevLett.113.020401.

[73] S. Ejima and H. Fehske, "Entanglement properties of the nontrivial haldane insulator in the 1d extended bose-hubbard model", Journal of Physics: Conference Series **592**(1), 012134 (2015), URL http://stacks.iop.org/1742-6596/592/i=1/a=012134.

[74] J. Towns, T. Cockerill, M. Dahan, I. Foster, K. Gaither, A. Grimshaw, V. Hazlewood, S. Lathrop, D. Lifka, G. D. Peterson, R. Roskies, J. R. Scott, and N. Wilkins-Diehr, "Xsede: Accelerating scientific discovery", Computing in Science & Engineering **16**(5), 62–74 (2014), DOI: doi.ieeecomputersociety.org/10.1109/MCSE.2014.80.

[75] M. Nakamura, "Tricritical behavior in the extended hubbard chains", Phys. Rev. B **61**, 16377–16392 (2000), DOI: 10.1103/PhysRevB.61.16377, URL http://link.aps.org/doi/10.1103/PhysRevB.61.16377.

[76] T. Giamarchi, *Quantum Physics in One Dimension*, (Oxford Univ. Press, Oxford, UK, 2004).

[77] D. Sénéchal, *An Introduction to Bosonization*, (Springer New York, New York, NY, 2004), DOI: 10.1007/0-387-21717-7_4, URL https://doi.org/10.1007/0-387-21717-7_4.

[78] J. Voit, "Phase diagram and correlation functions of the half-filled extended hubbard model in one dimension", Phys. Rev. B **45**, 4027–4042 (1992), DOI: 10.1103/PhysRevB.45.4027, URL https://link.aps.org/doi/10.1103/PhysRevB.45.4027.

[79] M. Tsuchiizu and A. Furusaki, "Ground-state phase diagram of the one-dimensional half-filled extended hubbard model", Phys. Rev. B **69**, 035103 (2004), DOI: 10.1103/PhysRevB.69.035103, URL https://link.aps.org/doi/10.1103/PhysRevB.69.035103.

[80] S. Fujimoto and N. Kawakami, "Competition between the mott transition and anderson localization in one-dimensional disordered interacting electron systems", Phys. Rev. B **54**, R11018–R11021 (1996), DOI: 10.1103/PhysRevB.54.R11018, URL https://link.aps.org/doi/10.1103/PhysRevB.54.R11018.

[81] R. Shankar, "Renormalization-group approach to interacting fermions", Rev. Mod. Phys. **66**, 129–192 (1994), DOI: 10.1103/RevModPhys.66.129, URL https://link.aps.org/doi/10.1103/RevModPhys.66.129.

[82] J. M. Kosterlitz and D. J. Thouless, "Ordering, metastability and phase transitions in two-dimensional systems", Journal of Physics C: Solid State Physics **6**(7), 1181–1203 (1973), DOI: 10.1088/0022-3719/6/7/010.

[83] J. M. Kosterlitz, "The critical properties of the two-dimensional xy model", Journal of Physics C: Solid State Physics **7**(6), 1046–1060 (1974), DOI: 10.1088/0022-3719/7/6/005.

[84] E. H. Fradkin, *Field Theories of Condensed Matter Physics*, volume 82, (Cambridge Univ. Press, Cambridge, UK, 2013).